Journal of Materials Chemistry C

REVIEW

View Article Online
View Journal | View Issue

Cite this: J. Mater. Chem. C, 2019, 7, 8753

Gallium oxide solar-blind ultraviolet photodetectors: a review

Jingjing Xu, Wei Zheng * and Feng Huang *

In recent years, solar-blind ultraviolet (UV) photodetectors have attracted significant attention from researchers in the field of semiconductor devices due to their indispensable properties in the fields of high-temperature event monitoring, anti-terrorism, security and *ad hoc* network communication. As an important member of the third-generation semiconductors, β-Ga_2O_3 is considered to be one of the most promising candidates for solar-blind UV detectors due to its ultra-wide band gap (~4.9 eV), economic efficiency, high radiation resistance and excellent chemical and thermal stability. Herein, we provide a comprehensive review on Ga_2O_3-based solar-blind UV photodetectors, with a detailed introduction of the developmental process of material growth methods and device manufacturing in the past decade. We classify the currently reported Ga_2O_3-based solar-blind UV photodetectors (mainly including photoconductive detectors, heterogeneous PN junction detectors and Schottky junction detectors) and summarize their respective superiorities and potentials for improvement. Finally, considering the actual application requirements, we put forward some meaningful suggestions, including energy band engineering and homogeneous epitaxy, for the future development of Ga_2O_3 material growth and device manufacturing.

Received 17th April 2019,
Accepted 3rd June 2019

DOI: 10.1039/c9tc02055a

rsc.li/materials-c

1 Introduction

More than 99% of the solar radiation spectrum is between the wavelengths of 150 and 4000 nm. In this band, about 7% important wavelengths are in the ultraviolet spectral region. According to different classifications, the ultraviolet light region can be subdivided into different regions, as shown in Fig. 1.

With a thickness of about 32 km (from 18 km to 50 km above sea level), the stratosphere, the atmosphere situated between the troposphere and the mesosphere, accommodates about 90% of the ozone in the atmosphere; moreover, it is the main region that absorbs solar vacuum and deep ultraviolet photons.[1–3] Near the surface, after being absorbed by the ozone layer, the solar ultraviolet photons with a wavelength less than 280 nm are very few and can be neglected;[4–6] the closer the photons to the surface and the smaller the wavelength, the more significant the reduction in the number of corresponding photons.[7] Therefore, the solar-blind ultraviolet ray refers to the ultraviolet light with the specified wavelength range of 200–280 nm,[8] which also endows the solar-blind ultraviolet detection technology with some inherent advantages such as low background noise, high sensitivity and strong anti-interference ability; this indicates the application potential of the solar-blind ultraviolet detection technology in the new generation of short-distance communication.[9] In addition to communications, the solar-blind UV detection technology is promising in the fields of people's livelihood including power grid safety monitoring, medical imaging, life science, and environmental and biochemical testing.[10,11]

Many attempts have been made to find suitable materials for the construction of solar-blind UV detectors; experiments have shown that β-Ga_2O_3 is one of the most preferred materials for the fabrication of solar-blind UV detectors. Ga_2O_3 is a kind of III–VI wide band gap semiconductor material, with the band gap E_g falling in the range of 4.7–4.9 eV, possessing excellent chemical and thermal stability. In addition, the ultra-wide band gap of Ga_2O_3 makes its absorption cut-off edge (260–280 nm) right around 280 nm, enabling better detection of solar-blind ultraviolet light. Ga_2O_3 also has the outstanding advantages of shorter absorption cut-off edge and lower growth cost. Its Baliga figure ($\varepsilon\mu E_g^3$, relative to Si) is as high as 3214.1, which is about 10 times that of SiC and 4 times that of GaN. This means that the devices developed with β-Ga_2O_3 will have smaller conduction losses and higher power conversion efficiency and thus have good application prospects in high-voltage and high-power devices.

In this article, we explored different types of Ga_2O_3-based solar-blind UV detectors and traced their development. Moreover, we reviewed the recent progress of solar-blind UV detectors and discussed the issues to be solved in this field as well as the

State Key Laboratory of Optoelectronic Materials and Technologies, School of Materials, Sun Yat-sen University, Guangzhou 510275, China. E-mail: zhengw37@mail.sysu.edu.cn, huangfeng@mail.sysu.edu.cn

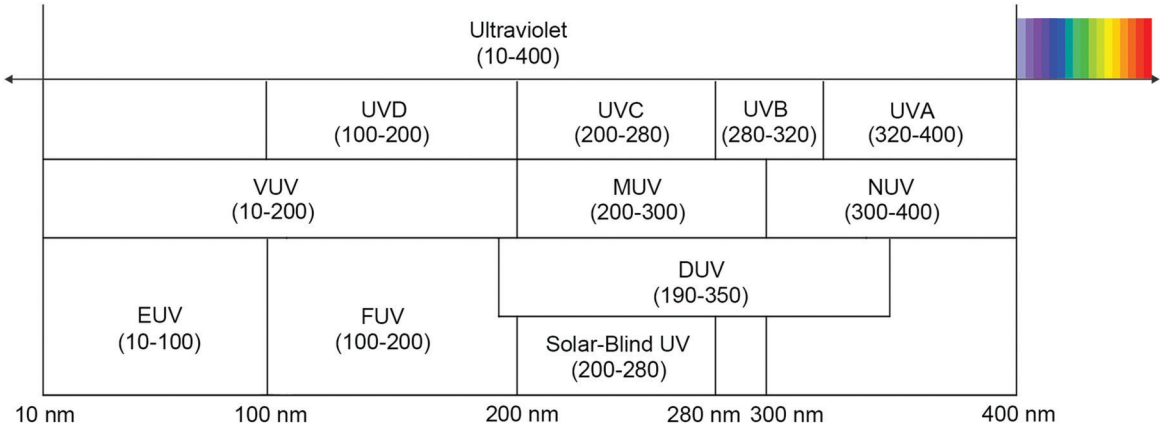

Fig. 1 Subdivision diagram of the ultraviolet light region.

future optimized attempts and predictions for solar-blind UV detectors.

2 General theory of ultraviolet detectors

2.1 Classifications and parameters of detectors

In recent years, photodetectors, devices that can convert optical signals into electrical signals or others, have been widely used in the field of science and technology. In the visible or near-infrared bands, they are mainly used for ray measurement and detection, industrial automation control, photometric measurement, *etc.*; on the other hand, in the infrared band, they are mainly used for missile guidance, infrared thermal imaging, infrared remote sensing and so on. The photoelectric effect utilized by photodetectors can be divided into external photoelectric effect and internal photoelectric effect. In the external photoelectric effect, photons excite a photocathode to generate photoelectrons, which are then obtained by an external electrode. The obtained optical signal (current, *etc.*) is the received radiation conversion value. The external photoelectric device usually refers to a photosensitive electro-vacuum device mainly used in ultraviolet, infrared and near-infrared bands. The internal photoelectric effect is divided into photoconductive effect and photovoltaic effect. In the photoconductive effect, after the semiconductor absorbs photons of sufficient energy, some of the electrons or holes are activated from the originally non-conductive bound state to the free state capable of conducting electricity; this results in an increase in semiconductor conductivity and a decrease of resistance in the circuit. In the photovoltaic effect, the photo-generated charge produces a small P–N potential difference across the junction within the semiconductor. The generated photo-voltage is amplified by photoelectric devices and can be directly measured. The devices based on photoconductive effects and photovoltaic effects are called photoconductive detectors and photovoltaic detectors, respectively.

In addition, ultraviolet light detectors can be divided into photo-thermal detectors and photodetectors. Photo-thermal detectors first convert optical signals into thermal signals through photo-thermal conversion and then convert thermal signals into electrical signals through thermoelectric conversion, finally outputting the changed electrical parameters. Since the surface coating of devices absorbs light radiation, the thermal effect is independent of wavelength, and thus, the sensitivity of photo-thermal detectors is not high. On the basis of traditional classification, there is another kind of detectors called photographic detectors. Although this kind of detectors have great advantages in image storage, they also have many disadvantages: low sensitivity, limited dynamic range, difficulty to eliminate the background fog level and so on. Herein, the abovementioned types of detectors are referred to photodetectors, which can be subdivided into several different types. Moreover, this study focuses on the discussion of photoconductive detectors and photovoltaic detectors.

After a long-time exploration of photodetectors, researchers have developed a mature system of detector evaluation indicators. The performance parameters include quantum efficiency, gain, responsivity, dark current, response time, noise equivalent power, detectivity, and normalized detectivity of photodetectors. According to the special requirements of devices, researchers can choose an appropriate combined system of parameters.

2.1.1 Quantum efficiency, gain and responsivity. Quantum efficiency is used to characterize the sensitivity of a device towards optical radiation. It is typically defined as the percentage of photons received on the light-receiving surface that are converted into electron–hole pairs. Quantum efficiency is also divided into external quantum efficiency, η, and internal quantum efficiency, η_0. External quantum efficiency corresponds to the external photoelectric effect, in which the metal surface releases electrons by absorbing the energy of the photon flux, and the corresponding devices can be called photo-emissive devices; on the other hand, internal quantum efficiency corresponds to the internal photoelectric effect, in which by absorbing incident photons, the metal excites the electrons from the valence band to the conduction band to form electron–hole pairs, and the corresponding devices can be called semiconductor devices. There is a certain

relationship between the external quantum efficiency η and the internal quantum efficiency η_0:[12]

$$\eta = \frac{\eta_0(1-r)[1-\exp(\alpha t)]}{1-r\exp(-\alpha t)}$$

where r represents the surface reflection coefficient, and α is the absorption coefficient.

The gain g is defined as the number of carriers generated by each electron–hole pair, that is, the ratio of output signals to input signals, which can also reflect the photosensitivity of devices. In general, the quantum efficiency and gain of a device can be speculated to a certain value. The quantum efficiency η along with the gain g determines the magnitude of current responsivity.[12] The definition equation of g is as follows:

$$g = \log_{10}(P_{out}/P_{in})$$

where P_{out} is the power of output signals, and P_{in} is the power of input signals.

Responsivity can be divided into the general responsivity R, frequency responsivity R_f, and spectral responsivity R_λ,[13,14] each of which has its own current and voltage; however, the current responsivity is more commonly used, with the unit of A W^{-1}.[15] The general responsivity R can also be referred to as sensitivity, defined as the ratio of the average output current/voltage to the average input power, which characterizes the average photoelectric conversion capability of a device. The frequency responsivity characterizes the photoelectric conversion capability of a device under the illumination of a particular frequency, f. Similarly, spectral responsivity characterizes the photoelectric conversion capability of a device at the specific wavelength of λ. The reason why this indicator exists is that most devices have spectral selectivity. The formula for calculating the spectral current responsivity $R_I(\lambda)$ is presented as follows:[12,16,17]

$$R_I(\lambda) = \frac{\lambda\eta}{hc}qg$$

where η is the quantum efficiency, λ is the wavelength, h is the Planck constant, c is the speed of light, q is the quantity of charge, and g is the photocurrent gain.

2.1.2 Dark current, photocurrent and response time. Dark current refers to the tiny current that is still generated on a device when no photons pass through photodetectors (such as photomultipliers, photodiodes, and charge-coupled devices). Dark current includes radiation current and saturation current of semiconductor junctions. The dark current is caused by the random generation of electrons and holes in the depletion layer of devices. The generation of dark current is related to specific defects of the depletion layer, which reflects the choiceness of devices to a certain extent. To obtain devices of high signal-to-noise ratio, the dark current should be controlled at a low level.[18]

In theory, photocurrent is generated by photons; when a photon with sufficient energy strikes the photodetector, an electron is excited; this will generate an electron–hole pair; if the absorption of photons occurs in the depletion layer, the internal electric field in this region will eliminate the barrier between the electrons and holes such that holes can move towards the anode and electrons can move towards the cathode; thus, the photocurrent is generated. In fact, the measured photocurrent is a combination of dark current and light-generated current, which also shows that the dark current must be minimized to improve the sensitivity of devices towards the light.

When photons are irradiated on photoelectric devices, devices do not change instantaneously with changes in external conditions because carrier migration takes time. This transit time becomes the response time. In general, response time is divided into two parts: rise time and decay time. The rise time can be defined as the time required for the photocurrent of devices to increase from 10% to 90% of the maximum value; similarly, the decay time can be defined as the time to reduce the photocurrent of devices from 90% of the highest value to 10%.[16,19]

2.1.3 Signal-to-noise ratio, noise equivalent power and detectivity. The minimum radiation power of all detectors is limited by the presence of noise. Noise is divided into radiation noise and internal noise of detectors. Radiation noise is further divided into signal fluctuation noise and background fluctuation noise. There are two basic ways to generate radiation noise: the fluctuation of free carrier velocity caused by random thermal motion, and the fluctuation of free carrier density caused by the randomness of thermal generation and thermal recombination rates.

The signal-to-noise ratio (SNR) is used to characterize the relative intensity of the required signal relative to the background noise, which is defined as the ratio of useful signal power to noise power, or the ratio of the square of their signal amplitudes. In addition, the common expression of the signal-to-noise ratio is described in dB units as follows:

$$\mathrm{SNR(dB)} = 10\log_{10}\frac{P_{signal}}{P_{noise}} = 20\log_{10}\frac{A_{signal}}{A_{noise}}$$

where P_{signal} is the power of the signal, P_{noise} is the power of noise, A_{signal} is the amplitude of signal, and A_{noise} is the amplitude of noise.

Noise equivalent power (NEP) is defined as the incident optical power required when the signal-to-noise ratio is one. For a photodiode, the noise equivalent power is approximately equal to its minimum detectable input power. Another parameter related to the noise equivalent power is detectivity (D), which is defined as the reciprocal of noise equivalent power. Since detectivity is proportional to the effective area A of detectors and the square root of the bandwidth Δf of amplifiers, to eliminate the abovementioned effects, the normalized detectivity D^* is derived as follows:[20]

$$D^* = D\cdot(A\cdot\Delta f)^{1/2}$$

2.2 Development of UV detector materials

Traditionally, research on solar-blind UV detector materials has focused on single-crystal thin films, including SiC,[21] diamond,[22,23] AlN,[24–26] BN,[17,27] and GaN.[28] However, detectors based on these materials are difficult to obtain due to technical difficulties in achieving high-quality single crystals of these materials; on the other hand, either because the cost is

significantly high and the economic benefits are significantly low, or because the band gap is not ideal, only some bands[21,22,24,29] of solar-blind ultraviolet detectors can be covered. At present, the research materials of solar-blind UV detectors are mainly concentrated on the following wide-band gap semiconductors that are sensitive to the solar-blind ultraviolet band: $Al_xGa_{1-x}N$,[29,30] $Mg_xZn_{1-x}O$[31–33] and monoclinic Ga_2O_3. $Al_xGa_{1-x}N$ and $Mg_xZn_{1-x}O$ belong to the band control range, and this article is mainly focused on solar-blind UV photodetectors based on Ga_2O_3.

Ga_2O_3 has five isomers, namely α, β, γ, ε and δ-Ga_2O_3. Among them, β-Ga_2O_3 is the most stable isomer, with the band gap of 4.7–4.9 eV. The other isomers are metastable. After a sufficiently long time or at a certain temperature, they will be converted into stable β-Ga_2O_3. β-Ga_2O_3 is considered as a new kind of transparent conductive oxides. All the Ga_2O_3 materials discussed in this article are in the β-Ga_2O_3 phases unless otherwise specified, and this information has not been provided hereinafter.

3 Ga_2O_3 solar-blind UV photodetectors

3.1 Photoconductive Ga_2O_3 detectors

The photoconductive effect is one of the internal photoelectric effects. It is a general term for the phenomena of photoelectric alterations that cause changes in the electrical properties of certain objects after they are irradiated by light. Generally, a photoconductor consists of a semiconductor channel and two ohmic contacts, with the ohmic contacts at both ends being present as source/drain electrodes.[34] When a bias voltage is applied to the photoconductor, there will be a small current between electrodes in a dark environment, namely the dark current; when the photon energy $h\nu$ at a certain wavelength of light irradiation is equal to or greater than the bandgap width E_g of semiconductors, photons can excite the electrons from the valence band to the conduction band, thereby generating conductive electron–hole pairs, increasing the conductivity of semiconductors as well as outputting electrical signals. Note that the photocurrent may gradually decay due to carrier recombination on the semiconductor surface and/or in the bulk.[34]

Among all types of detectors, photoconductive detectors are most widely studied due to their convenience. In photoconductive detectors, low-resistance photoconductors usually work in constant-current circuits. Compared with the sample resistance, the series load resistance is larger, and the voltage changes generated at both ends of the sample can be used as detection signals. For high-resistance photoconductors, a constant-voltage circuit is preferred, and the current changes in the bias circuit can be used as signals for detection.[12]

To detect the solar-blind UV photosensitivity of Ga_2O_3, some researchers have carried out experiments on Ga_2O_3 films and nanostructures. In 2006, Ji *et al.*[35] used the method of pulse spray pyrolysis to deposit the Ga_2O_3 films from the $GaCl_3$ ethanol solution. The film had the transmittance of more than 80% to light with wavelength greater than 275 nm. The dark resistance of the film was about 12 kΩ, which was insensitive to sunlight ($\lambda > 285$ nm) but had an obvious resistance change (8 kΩ) for the light of 254 nm. In the same year, using N_2 gas as a carrier, Feng *et al.*[36] applied the evaporation method to grow Ga_2O_3 nanowires on Si substrates coated with 10-nm Au at 980 °C for 1 hour. A single nanowire was then placed on the Au electrode with the thickness of about 50 nm to form the Au–Ga_2O_3–Au photodetector structure. The dark current of the device was about 10^{-12} A. Under the illumination of 254 nm ultraviolet light, the conductivity increased by three orders of magnitude (from the pA level to the nA level), and the response time of the rising and falling edges was 0.22 and 0.09 s, respectively. It has been further verified by the above-mentioned experiments that Ga_2O_3 shows obvious photosensitivity to solar-blind ultraviolet light in both the film and the nano-meter morphology.

3.1.1 Film-based detectors. To improve the performance of photoconductive detectors, researchers have tried a variety of methods to grow Ga_2O_3 films. The most common methods are molecular beam epitaxy (MBE),[37–46] metal oxide chemical vapor deposition (MOCVD)[47–56] and radio frequency magnetron sputtering (RFMS).[57–60] In addition, there are several other methods for growing the Ga_2O_3 films such as sol–gel,[61,62] oxidation,[63–66] pulsed laser deposition (PLD),[67] microwave irradiation[68] and atomic layer deposition (ALD).[69]

As one of the most common growth methods for Ga_2O_3 films, the molecular beam epitaxy (MBE) method has become more sophisticated over time, which thus improves the performance of solar-blind UV detectors based on Ga_2O_3 films. In the process of fabrication of the Ga_2O_3 films, the substrates used are mainly sapphire[37,40,41,45,46] and Al_2O_3.[38,39,43,44] In 2016, Liu *et al.*[40] deposited Ga_2O_3 films from the vapor Ga in a standard shuttered Knudsen cell (K-cell) and mono-atomic oxygen. In addition, they introduced a homo-self-templated buffer layer during the growth of the Ga_2O_3 films to improve the device performance. Finally, the detector exhibited a high photo-responsivity (259 A W^{-1}) and high external quantum efficiency (7.9×10^4%), with dark current at the level of 10^{-11} and the light–dark ratio of 10^4 level (Fig. 2).

MOCVD is a kind of CVD technology that uses a thermal decomposition reaction of an organic metal to conduct the vapour-phase epitaxial growth of the thin film. In 2018, Zhang *et al.*[51] deposited the Ga_2O_3 films on *c*-plane sapphire substrates at 800 °C using the method of MOCVD. Compared to the case of traditional O_2 depositional setting, the research team introduced N_2O to reduce the scattering/trapped centre of photo-generated carriers and thus obtain high-performance solar-blind UV photodetectors. Under the 10 V bias, the photo-responsivity of the detector was as high as 26.1 A/W, the on/off ratio ($I_{255\,nm\,light}/I_{dark}$) increased to 10^4, and the rise/decay response time was 0.48/0.18 s.

RFMS is a combination of magnetron sputtering and radio frequency sputtering. Due to its unique advantages of high speed, simple equipment and high-quality coating, it has been rapidly developed and applied in the field of solar-blind UV detectors. In 2018, Peng *et al.*[60] used the method of radio

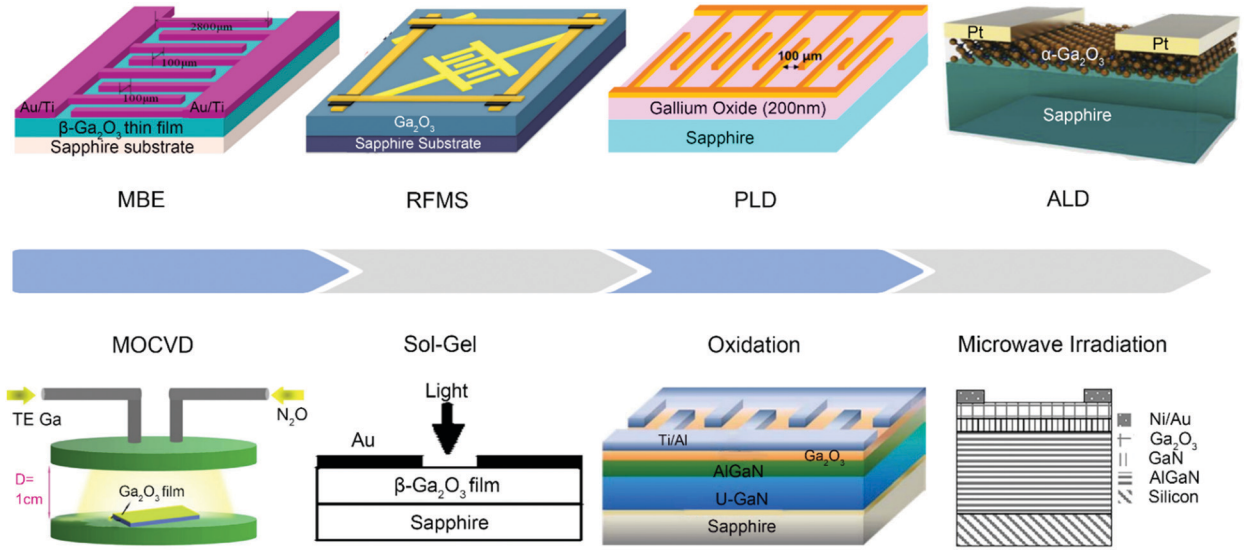

Fig. 2 Schematic of different methods used to grow thin-film photodetectors: MBE, RFMS, PLD, ALD, MOCVD, sol–gel, oxidation and microwave irradiation. Reproduced with permission from ref. 39 Copyright 2014 AIP Publishing LLC, ref. 60 Copyright 2018 IEEE, ref. 67 Copyright 2015 Optical Society of America, ref. 69 Copyright 2018 Elsevier B.V., ref. 51 Copyright 2017 Elsevier B.V., ref. 61 Copyright 2007 American Institute of Physics, ref. 64 Copyright 2013 IEEE and ref. 68 Copyright 2018 Author(s).

frequency magnetron sputtering to plate a 200 nm-thick Ga_2O_3 film on a 2-inch (0001) Al_2O_3 substrate after standard treatment. In addition, the research team first designed metal–semiconductor–metal (MSM) photodetectors with a square array (32 × 32, 16 × 16, 8 × 8 and 4 × 4) on the basis of the Ga_2O_3 thin films. Taking the 4-1 photodetector cell in 4 × 4 photodetector arrays as an example, the photo-responsivity of the detector reached 8.926×10^{-1} A W^{-1} at the 10 V bias voltage, corresponding to the quantum efficiency of 444%. Other photodetector cells also exhibit solar-blind UV photoelectric properties, showing the same photo-responsivity within the standard deviation of 12.1% (Fig. 3).

In other growth methods, researchers have also tried unique improvements. In 2007, based on the Ga_2O_3 films grown by the sol–gel method, Kokubun *et al.*[61] fabricated planar geometry photoconductive detectors; in 2013, *via* furnace oxidation, Huang *et al.*[64] made the Ga_2O_3/AlGaN/GaN three-band photodetector to measure the UV-A, UV-B and UV-C bands, respectively; in 2013, Huang *et al.*[65] prepared the Ga_2O_3 films by thermal oxidation and used them as the cap layer of the InGaN/GaN multiple quantum well to finally fabricate the MSM structure. In addition to the abovementioned methods, the Ga_2O_3 films have been grown *via* pulsed laser deposition[67] and microwave irradiation.[68] Moreover, atomic layer deposition[50] has been used to grow α-Ga_2O_3 films, and solar-blind ultraviolet photodetectors have been fabricated based on the corresponding films.

For photoconductive detectors, photo-responsivity, quantum efficiency, and response time are important performance indicators. To date, to the best of our knowledge, the photodetector fabricated by Liu *et al.*[40] in 2016, which was made of the Ga_2O_3 film on sapphire pre-seeded by a homo-self-templated buffer layer, achieved the best photo-responsivity of 259 A W^{-1} and optimal quantum efficiency of 7.9×10^4%. In 2019, the photodetector made by Lee *et al.*,[69] which was based on the α-Ga_2O_3 film grown *via* low-temperature atomic layer deposition, obtained best response time, with the optimal rise/decay response time of 539 ns/89 μs. However, it is not difficult to see that for Ga_2O_3 film-based solar ultraviolet photodetectors, good photo-responsivity and ideal response time are not well compatible, and further optimization schemes have to be pointed out (Table 1).

3.1.2 Bulk-based detectors. In the growth process, the growth of a Ga_2O_3 single crystal with high quality is a technical difficulty due to the problem of cracking and polycrystallization.[72,73] In 2008, Aida *et al.*[72] have successfully employed an edge-defined, film fed growth (EFG) method to grow 2-inch Ga_2O_3 crystals; this method makes it possible to fabricate bulk Ga_2O_3-based solar-blind UV detectors.

In most of the experiments, the growth of Ga_2O_3 crystals was completed on heterogeneous substrates. Therefore, the comparison between Ga_2O_3 crystals grown on homogenous substrates and those grown on heterogeneous substrates is of great significance. In 2016, Feng *et al.*[74] used the EFG technique and Ga_2O_3 with the purity of 99.99% as a raw material to grow large-size Ga_2O_3 crystals on a (100)-oriented intrinsic Ga_2O_3 bulk substrate and compared them with the Ga_2O_3 crystals grown on sapphire substrates. The experimental results show that at the bias voltage of 40 V, the responsivity of the former (0.05 A W^{-1}) was significantly higher than that of the latter (~0.009 A W^{-1}), and the response time of the former (0.45 s/0.24 s) was similar to that of the latter (0.40 s/0.18 s). After a comprehensive comparison, the performance of the Ga_2O_3 crystals grown on homogeneous substrates was found to be better.

In 2017, Mu *et al.*[73] employed the EFG method and Ga_2O_3 with the purity of 99.99% as a raw material to grow Ga_2O_3 single crystals by a radio source induction furnace and then obtained

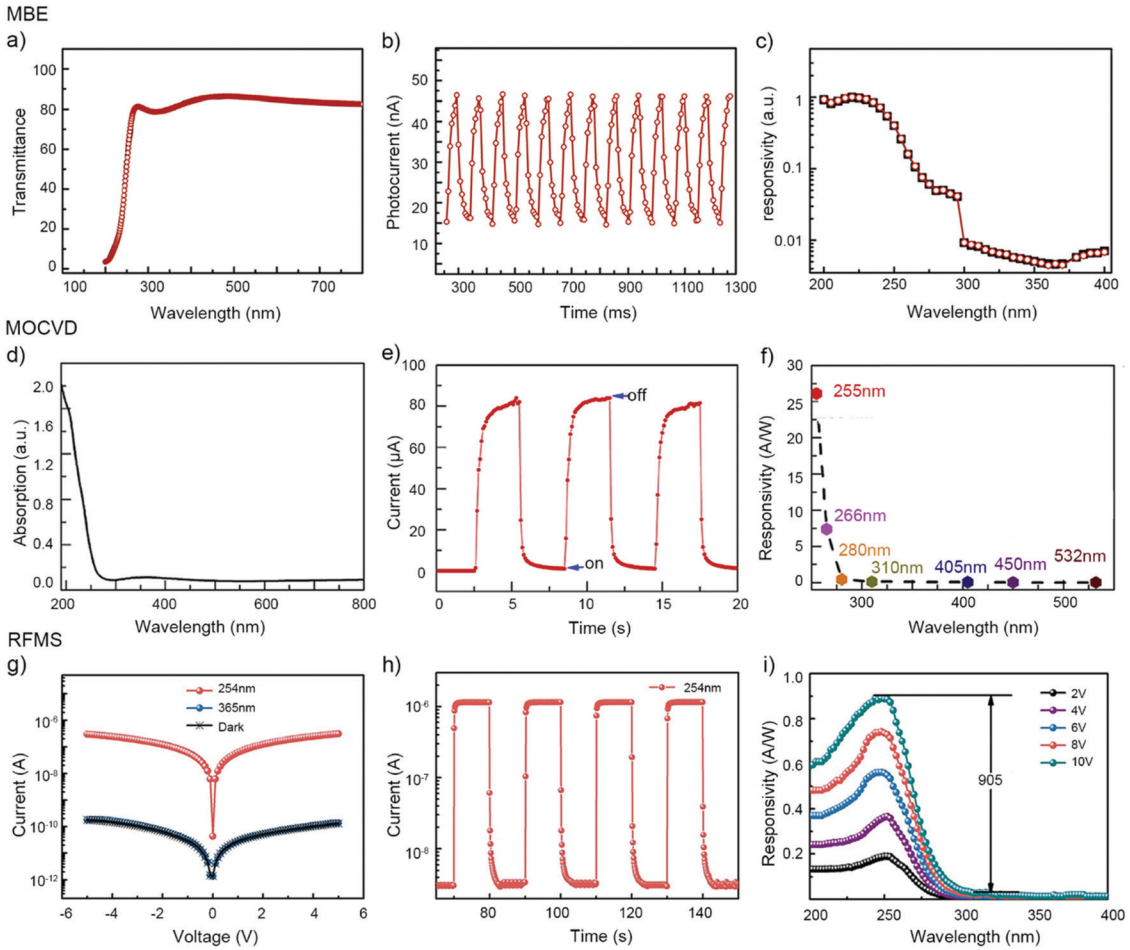

Fig. 3 (a) Optical transmittance spectrum of the Ga_2O_3 thin films, (b) transient response and (c) spectral response of the photodetectors made from the Ga_2O_3 thin films. Reproduced with permission from ref. 40 Copyright 2015 Elsevier B.V. (d) Absorption spectrum of the Ga_2O_3 films, (e) time-dependent photocurrent and (f) spectral response of detectors. Reproduced with permission from ref. 51 Copyright 2017 Elsevier B.V. (g) The *I*–*V* characteristics curves, (h) time-dependent photo-response and (i) spectral response at room temperature for the photodetectors fabricated with the Ga_2O_3 films. Reproduced with permission from ref. 60 Copyright 2018 IEEE.

large-sized Ga_2O_3 wafers with high surface quality by simple mechanical exfoliation to manufacture MSM photodetectors. During the growth process, the research team solved the problems of cracking and polycrystallization during the growth of Ga_2O_3 using a high-quality 1-inch-wide seed. As a result, the responsivity of 0.003 A W^{-1} was obtained under the bias voltage of 40 V, and the decay time was 0.14 s (Fig. 4).

3.1.3 Micro/nanostructure-based detectors. For the development of Ga_2O_3-based solar-blind UV photodetectors, thin-film-based PDs have been widely studied for their convenience and diversity of methods; however, lower responsivity limits their practical application. On the other hand, the practicality of bulk Ga_2O_3-based photodetectors is affected due to the high cost of manufacturing methods. Therefore, researchers have tried to solve this problem using photodetectors based on Ga_2O_3 micro-nanostructures. Compared to their bulk or thin film counterparts, the nanostructures have already displayed superior sensitivity to light in devices due to their high surface-to-volume ratios, Debye length comparable to their small size and superior stabilities owing to perfect crystallinities.[23,27]

At present, researchers have applied a variety of methods (*e.g.*, chemical vapor deposition,[76,77] oxidation,[78,79] direct evaporation,[36] vapor–liquid–solid,[80] vapor phase transport,[81] laser molecular beam epitaxy[82] and mechanical exfoliation[83]) to synthesize multiple micro-nano morphological structures (*e.g.*, nanowire,[36] nanobelt,[77] nanosheet,[79] nanoflower,[84] and microflake[83]) and further explored and discussed their structures and electrical properties (Table 2).

In nanostructures, the morphology of nanowires is most widely studied. Compared to the devices based on traditional nanowire structures, bridged nanowire devices have many advantages such as an efficient and simple preparation process, small surface contamination of nanowires and good electrical performance. In 2010, Li *et al.*[76] used the method of one-step CVD to prepare the Ga_2O_3 bridged nanowire structure with a stable photocurrent (photocurrent fluctuation $<3\%$). The detector had the light–dark ratio of 3×10^4, and the decay time was $\tau \ll 20$ ms under 254 nm light illumination. In addition, the research team first observed the intrinsic UVC emissions of Ga_2O_3 nanowires. By adjusting different growth

Table 1 Parameter summary list of photoconductive film-based Ga_2O_3 detectors

Growth Method	Type	Bias (V)	Photo-responsivity (A W^{-1})	Quantum efficiency (%)	Rise time (s)	Decay time (s)	Ref.	Time
MBE	Ga_2O_3 film	10	0.037	18			37	2007
	Ga_2O_3 film	10			0.86	1.02	38	2014
	Ga_2O_3 film				0.62	0.83	39	2014
	Ga_2O_3 film	20	259	79 000			40	2016
	Ga_2O_3 film						41	2016
	Mn:Ga_2O_3 film	10	0.07	36	0.91	0.28	42	2016
	α-Ga_2O_3 film	20	0.015	7.39			43	2016
	ε-$Ga_{1.8}Sn_{0.2}O_3$ film	15	0.00605	3.02			44	2016
	Ga_2O_3 film	4	>1.5		3.33	0.4	45	2017
	Ga_2O_3 film	20	153		5.0	10.3	46	2017
	Ga_2O_3 film	10	8.41		2.97	0.41	70	2019
MOCVD	Ga_2O_3 film	5					47	2013
	Ga_2O_3 film	20	17	8228			48	2015
	Ga_2O_3 film	5	1.45		0.58	1.2	49	2015
	Ga_2O_3 film	1	0.11		0.4	0.45	50	2017
	Ga_2O_3 film	1	0.14		0.3	0.2	50	2017
	Ga_2O_3 film	10	26	13 600	0.48	0.18	51	2018
	Ga_2O_3 film	6	12.8		0.0015	0.002	52	2018
	Ga_2O_3 film	20	150	73 900	1.8	0.3	53	2018
	Ga_2O_3 film	5	1.05	512	4.5	2.2	54	2018
	ε-Ga_2O_3 film	10			2	0.4	55	2018
	Ga_2O_3 film	10	1.2				56	2019
RFMS	Ga_2O_3 film	10	100				57	2016
	α-GaO_x film	10	70.26		0.41	0.04	58	2017
	Ga_2O_3 film	10	4.21		0.41	0.02	58	2017
	α-Ga_2O_3 film	10	0.19		0.000019	0.0000807	59	2017
	Ga_2O_3 film	10	0.8926	444	0.305	0.251	60	2018
Sol–Gel	Ga_2O_3 film	10	0.00008				61	2007
	Ga_2O_3 film	30	0.0013		0.1	0.1	62	2018
Oxidation	Ga_2O_3 film	5	0.453	>100			63	2011
	Ga_2O_3/AlGaN/GaN	3	10				64	2013
	Ga_2O_3/InGaN/GaN	5	10				65	2013
	Nanotextured Ga_2O_3	20	0.292	1.34	1.4	0.1	66	2017
PLD	Ga_2O_3 film	5	0.903				67	2015
	Ga_2O_3 film	10	0.74		0.193	0.2	71	2019
Microwave irradiation	Ga_2O_3film	22	0.1				68	2018
ALD	α-Ga_2O_3 film		0.76		0.00000054	0.000089	69	2019

temperatures to control the defect concentration in nanowires, they have found that the defects caused by oxygen vacancies and Ga vacancies have an important impact on the photo-response (Fig. 5).

Since two-dimensional (2D) semiconductors are limited to graphene analogues of layered materials, it is extremely challenging to fabricate 2D non-layered materials with thicknesses of only a few atomic layers.[79] In 2014, Feng *et al.*[79] successfully fabricated 2D Ga_2O_3 polycrystalline nano-sheets with a thickness of less than 10 nm by thermal oxidation of GaSe nano-sheets. The responsivity of the fabricated photodetectors was 3.3 A W^{-1} at 254 nm, and the external quantum efficiency was 1600%. Moreover, the unique advantages of photodetectors based on 2D Ga_2O_3 nanosheets include fast photoswitching, good stability and high responsivity, which indicate a new opportunity for the application of these photodetectors in solar-blind UV detectors.

Due to the degradation of dark current and photo-response characteristics, it is difficult to prepare solar-blind ultraviolet photodetectors operating in a high-temperature environment. In 2014, Zou *et al.*[85] first produced (100) facet-oriented Ga_2O_3 multi-layered nanobelts that could maintain good mechanical and electrical properties and high stability at high temperatures. The high-performance parameters obtained by the detector include a high photo-excited current (>21 nA), an ultralow dark current (below the detection limit of 10^{-14} A), a fast time response (<0.3 s), a high photo-responsivity ($\approx$851 A W^{-1}), and a high external quantum efficiency ($\sim 4.2 \times 10^3$); thus, the detector can have potential applications in photodetectors and optical switches operating in a high-temperature environment.

For the γ-Ga_2O_3 nanostructures that have been rarely studied, recently, researchers have found that they exhibit size-tunable photoluminescence.[87] In 2014, Teng *et al.*[84] prepared γ-Ga_2O_3 nanoflowers of metastable phase by a hydrothermal method. A simple solvothermal method was used to realize the morphology-controlled synthesis of γ-Ga_2O_3 nanostructures. The γ-Ga_2O_3 nanoflower-based solar-blind UV detector exhibits excellent photoelectric properties of large light–dark ratio and fast response speed (Fig. 6).

In addition to those based on nanostructures, photodetectors based on Ga_2O_3 micron structures have been applied in the field of solar-blind UV detectors. In 2017, Oh *et al.*[83] separated a Ga_2O_3 microflake from an unintentionally doped single crystalline Ga_2O_3 substrate *via* mechanical exfoliation and fabricated MSM-structured solar-blind UV detectors using graphene as an electrode. These detectors have excellent performance, with the

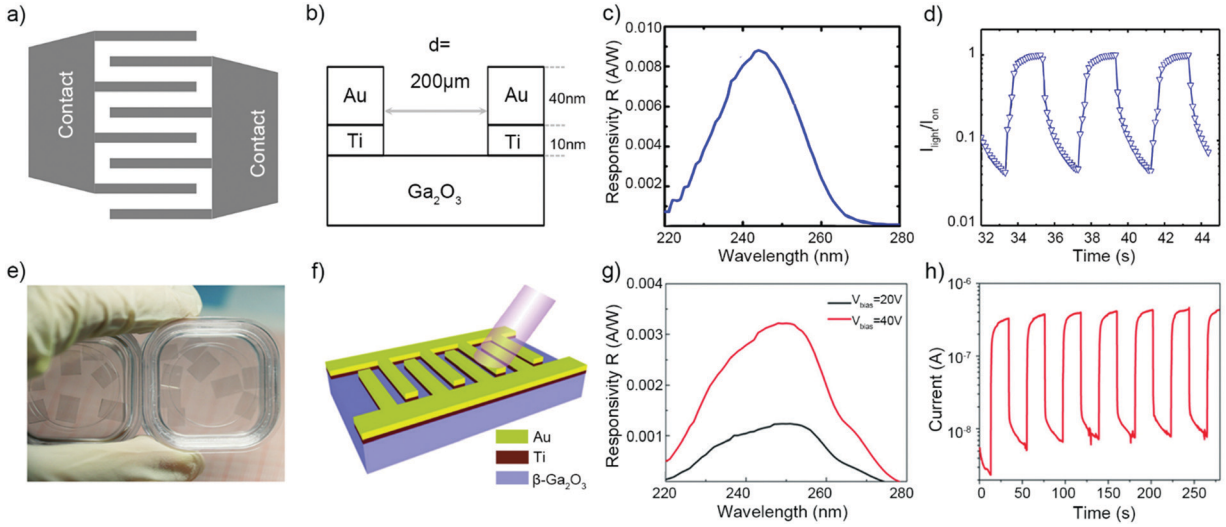

Fig. 4 (a) Top view and (b) cross-sectional schematic, (c) responsivity *versus* optical illumination λ and (d) time-dependent I_{light} of Ga_2O_3 photodetectors. Reproduced with permission from ref. 74 Copyright 2016 IEEE. (e) Epi-ready wafer image of the exfoliated crystal wafers, (f) schematic, (g) spectroscopic responsivity and (h) time response of MSM-structure photodetectors based on Ga_2O_3 single crystals. Reproduced with permission from ref. 73 Copyright 2017 Royal Society of Chemistry.

Table 2 Parameter summary list of photoconductive bulk-based Ga_2O_3 detectors

Type	Growth method	Bias (V)	Photoresponsivity (A W^{-1})	Rise time (s)	Decay time (s)	Ref.	Time
Bulk Ga_2O_3	EFG	40	0.05	0.45	0.24	74	2016
		40	0.003	4.4	0.14	73	2017
		5	0.23	0.00048	0.00038	75	2019

photo-responsivity of up to 29.8 A W^{-1}, the light–dark ratio of about 1×10^6%, and the detectivity of about 1×10^{12} Jones (Table 3).

3.2 Photovoltaic Ga_2O_3 heterojunction detectors

Photovoltaic effect refers to the phenomenon in which light causes a potential difference between uneven semiconductors or different junctions combined by semiconductors and metals. The built-in electric field induced by this potential difference is equivalent to the externally applied bias in photoconductors, which causes the separation of photo-induced electron–hole pairs. The junctions can be PN junctions composed of two kinds of semiconductors with opposite doping types or Schottky barrier junctions produced at the interface between a semiconductor and a metal with unmatched work functions. In the dark, the photodetectors working under the photovoltaic effect exhibit rectification characteristics, namely nonlinear *I–V* curve characteristics. In the case of a certain wavelength of light radiation and zero bias voltage, short-circuit current or short-circuit voltage will be formed in photovoltaic detectors due to the presence of the built-in electric field.

The Ga_2O_3 material has the wide band gap of about 4.9 eV; thus, essentially, it is an insulating material; however, it becomes an n-type semiconductor when it is grown under reducing conditions; this is attributed to oxygen deficits within the crystal lattice.[72,74] In addition, highly-conductive n-type Ga_2O_3 can be obtained by doping tetravalent elements such as Si and Sn. Therefore, the most common photodiode is the Ga_2O_3-based solar-blind UV heterogeneous PN junction photodiode, which is made of Ga_2O_3 as the n-type material.[90–92] Detectors operating under the photovoltaic effect should be self-powered, that is, their applied bias voltage should be 0 V (Fig. 7).

In this study, solar-blind UV photovoltaic devices have been generally divided into two categories: heterogeneous PN junction photodiodes and Schottky junction photodiodes.

3.2.1 Photovoltaic heterogeneous PN junctions. After determining that the n-type material was Ga_2O_3, the next step was to select the p-type material. To date, whether in the photovoltaic or the non-photovoltaic mode, many studies have been conducted on p-type materials such as GaN,[91,93,96,97] SiC,[98–100] Si,[101] ZnO,[94,102,103] Nb:$SrTiO_3$ (NSTO),[104] graphene,[105,106] diamond[95] and MoS_2;[107] however, a technological problem still exists for some of them. This section focuses on the discussion of some of the p-type materials and self-powered PN junction photodiodes combined with Ga_2O_3.

The transparency of high-quality GaN at a wavelength greater than the band gap (3.39 eV corresponding to 366 nm) makes it an ideal photodetector material as it can simultaneously maintain close to unit quantum efficiency in ultraviolet bands and repel the near-infrared and visible lights of the solar spectrum.[108] In 2017, Li *et al.*[93] deposited a Ga_2O_3 film on a 4 μm-thick Mg-doped p-type GaN film *via* pulse laser deposition technology and made photodiodes using In/Ag as electrodes.

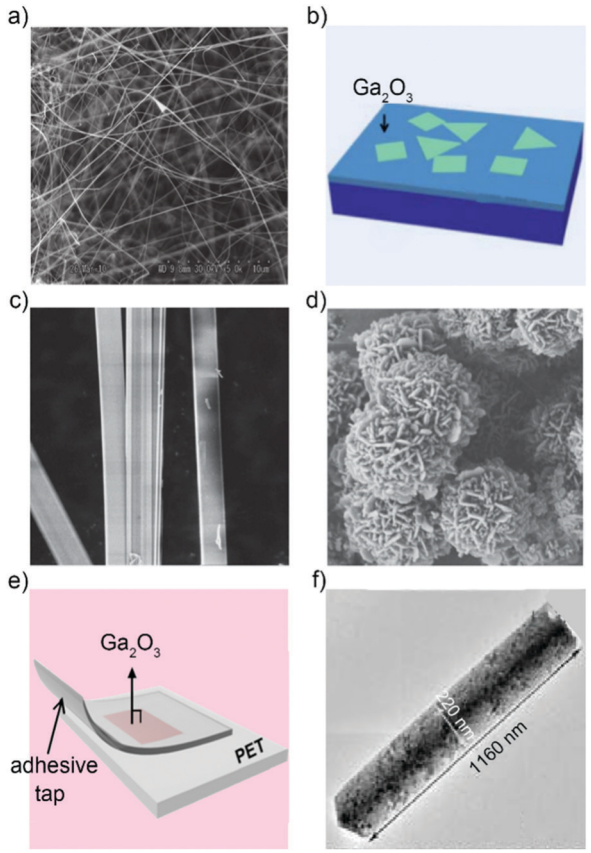

Fig. 5 (a) Nanowire, (b) nanosheet, (c) nanobelt, (d) nanoflower, (e) microflake, and (f) nanorod-structured Ga_2O_3-based solar-blind photodetectors. Reproduced with permission from ref. 76 Copyright 2010 WILEY-VCH Verlag GmbH & Co. KGaA, Weinheim, ref. 79 Copyright 2014 Royal Society of Chemistry, ref. 85 Copyright 2014 Wiley-VCH Verlag GmbH & Co. KGaA, Weinheim, ref. 84 Copyright 2014 WILEY-VCH Verlag GmbH & Co. KGaA, Weinheim, ref. 83 Copyright 2017 American Chemical Society and ref. 86 Copyright 2019 Royal Society of Chemistry.

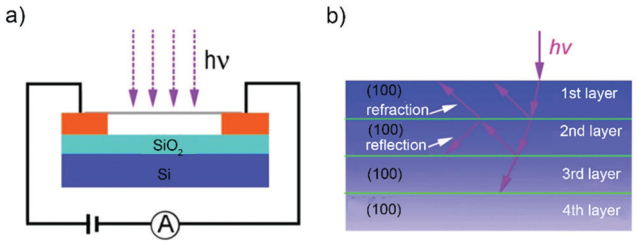

Fig. 6 (a) Schematic of Ga_2O_3 nanobelt photodetectors and (b) schematic of a model showing multiple reflection and refraction of electromagnetic waves. Reproduced with permission from ref. 85 Copyright 2014 Wiley-VCH Verlag GmbH & Co. KGaA, Weinheim.

The Ga_2O_3 film was experimentally measured to grow with orientation being along the $(\bar{2}01)$ lattice plane. At zero bias, the following results were obtained: the high responsivity of 54.43 mA W^{-1}, fast decay time of 0.08 s, high I_{light}/I_{dark} ratio of 152, and high detectivity of 1.23×10^{11} cm $Hz^{1/2}$ W^{-1}.

ZnO, having a very small lattice mismatch (<5%) with Ga_2O_3, is a good candidate to construct a heterostructure with Ga_2O_3. In 2017, Zhao *et al.*[94] synthesized ZnO–Ga_2O_3 core–shell heterostructure microwires and fabricated them into photodiodes, in which Ga_2O_3 was oriented along the $(\bar{2}01)$ lattice plane. To suppress the defects in the grain boundaries between two materials and thereby improve the performance of photodetectors, researchers have replaced the two-step CVD method[109] with a simple one-step CVD method.[94] At zero bias, the responsivity was measured to be 9.7 mA W^{-1} at 251 nm, the UV/visible rejection ratio ($R_{251\,nm}/R_{400\,nm}$) was 6.9×10^2, and the rise/decay time was less than 100 μs/900 μs.

Diamond and Ga_2O_3 have different work functions. After they are fabricated into heterojunctions, they may form a built-in electric field, which is beneficial to the self-powered property. In 2018, Cheng *et al.*[95] introduced diamond as a p-type material, and diamond wafers were homogenously grown on (100) diamond in a high-temperature and high-pressure environment. After this, using a plasma-enhanced CVD apparatus, Ga_2O_3 was deposited on the diamond wafer to form diamond/Ga_2O_3 heterojunctions. At the bias of 0 V, the peak responsivity of the heterojunctions was 0.2 mA W^{-1}, the cut-off wavelength was 270 nm, and its UV/visible suppression ratio exceeded two orders of magnitude, indicating good self-powered solar-blind UV detection properties of these heterojunctions (Fig. 8).

3.2.2 Photovoltaic Schottky junction. Schottky barrier photodiodes have been extensively studied and used as UV detectors. Compared to heterogeneous PN junction photodiodes, these devices show some additional advantages: simple fabrication, no high-temperature diffusion process and high-speed response.[12] Semiconductors or integrated circuits must be connected to external circuits. This connection is achieved by a non-rectifying contact between metals and semiconductors, namely the ohmic contact. In contrast, the Schottky barrier refers to the metal–semiconductor interface with rectifying properties. The biggest difference between the Schottky barrier and the PN interface is that the former has lower interface voltage and relatively thin (almost no) width of the depletion layer at the metal end.

In 2009, Oshima *et al.*[110] used transparent polystyrene sulfonic acid (POEDT-PSS) to form a Schottky contact with the semi-Ga_2O_3 high-resistance layer. Between them existed a semi-insulating layer, followed by an ohmic contact between n-type Ga_2O_3 and two In electrodes on the back side of the substrate. The 250 nm/300 nm rejection ratio of the device is about 1.5×10^4, which shows significant solar-blind photoelectric characteristics. The external quantum efficiency at 250 nm was about 18%, and the photo-response time was about 9 ms.

In 2016, Chen *et al.*[111] used the Ga metal as a raw material to grow Ga_2O_3 nanowire arrays by a simple thermal oxidation method and deposited a 20 nm-thick Au layer on them to prepare photodetectors of the Au/Ga_2O_3 nanowire Schottky-type vertical structure. The cut-off wavelength of the photoresponsivity of the device was about 270 nm, and the maximum photo-response was obtained at around 258 nm. The corresponding photo-responsivity was 0.01 mA W^{-1} at the bias voltage of 0 V, with a fast response time (the corresponding rise/decay time was approximately 1 μs/64 μs) and self-powered properties (Table 4).

Table 3 Parameter summary list of photoconductive micro/nanostructure-based Ga_2O_3 detectors

Type	Growth method	Bias (V)	Photo-responsivity (A W^{-1})	Quantum efficiency (%)	Rise time (s)	Decay time (s)	Ref.	Time
Ga_2O_3 nanowire	Direct evaporation	−8			0.22	0.09	36	2006
	MOCVD	50			≪0.02		76	2010
	Vapor–liquid–solid	10	0.0008	0.39			80	2010
		5	0.000372	0.18			88	2011
	Vapor phase transport	5	0.0034	1.37			81	2013
	LMBE	10	1.4		1.26	1.99	82	2016
	Thermal oxidization	5	0.185		0.009	0.008	78	2018
	CVD	25	0.71	246.6	0.37	0.19	89	2019
Ga_2O_3 nanobelt	CVD	30	37.6	187	11.8	<0.3	77	2011
			851	4200		<0.3	85	2014
Ga_2O_3 nanosheet	Furnace oxidation		3.3	1600			79	2014
γ-Ga_2O_3 nanoflower	Oxidation	0.5				<0.1	84	2014
Ga_2O_3 micro flake	Mechanical exfoliation		29.8				83	2017

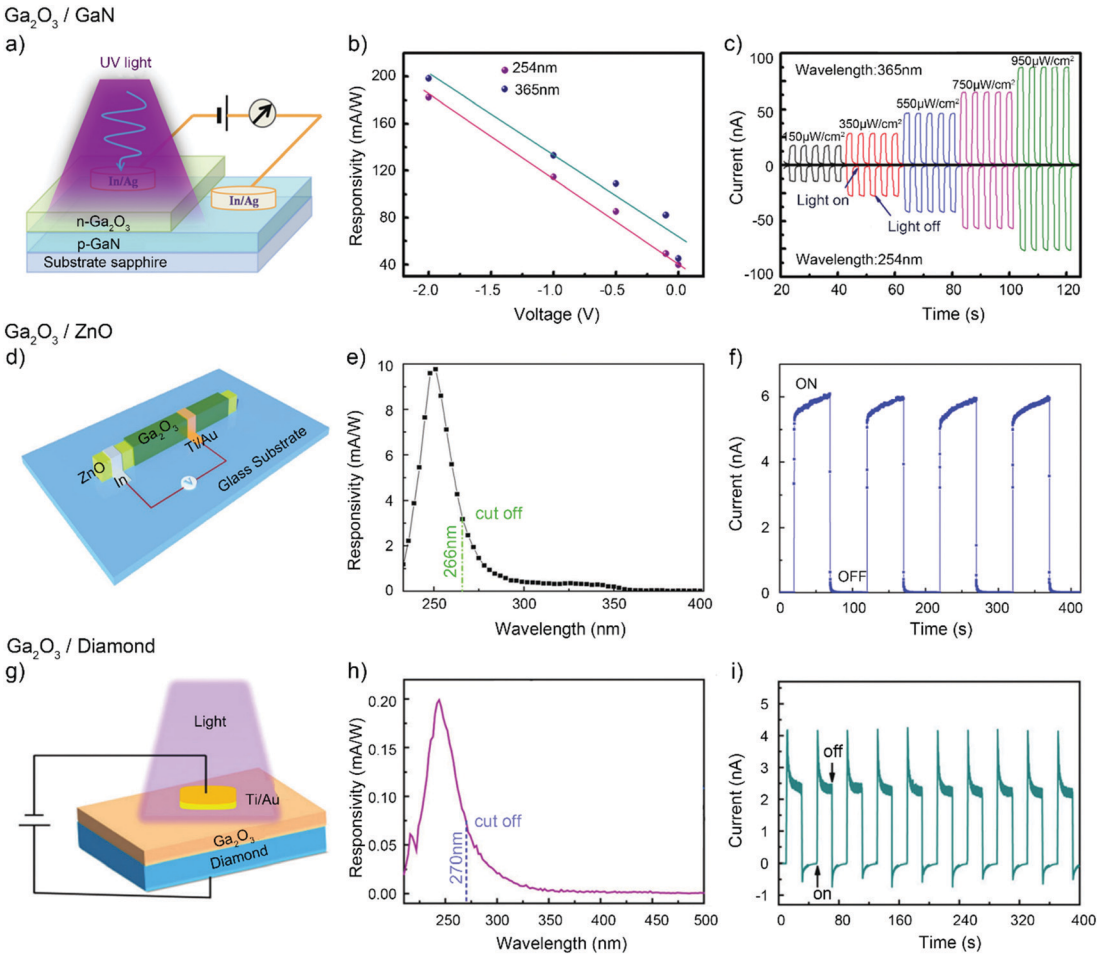

Fig. 7 (a) Schematic, (b) responsivity and (c) time-dependent photo-response of the fabricated prototype GaN/Ga_2O_3 PN junction photodetectors. Reproduced with permission from ref. 93 Copyright 2017 Royal Society of Chemistry. (d) Schematic, (e) photo-response spectrum and (f) time-response characteristics of heterojunction photodetectors. Reproduced with permission from ref. 94 Copyright 2017 WILEY-VCH Verlag GmbH & Co. KGaA, Weinheim. (g) Schematic, (h) photo-response spectrum and (i) time-resolved photocurrent of diamond/Ga_2O_3-based photodetectors. Reproduced with permission from ref. 95 Copyright 2018 Royal Society of Chemistry.

3.3 Non-Photovoltaic Ga_2O_3 heterojunction detectors

Photodiodes operating based on the photovoltaic effect usually have improved detectivity as well as maximum linearity and sensitivity due to the presence of minimal dark current; however, due to the lack of internal gain, their responsivity will be less than that of the photodetector operating based on the photoconductive effect. In addition to working under the photovoltaic effect, photodiodes can operate in the photoconductive mode, *i.e.* under bias voltage. Thus, the addition

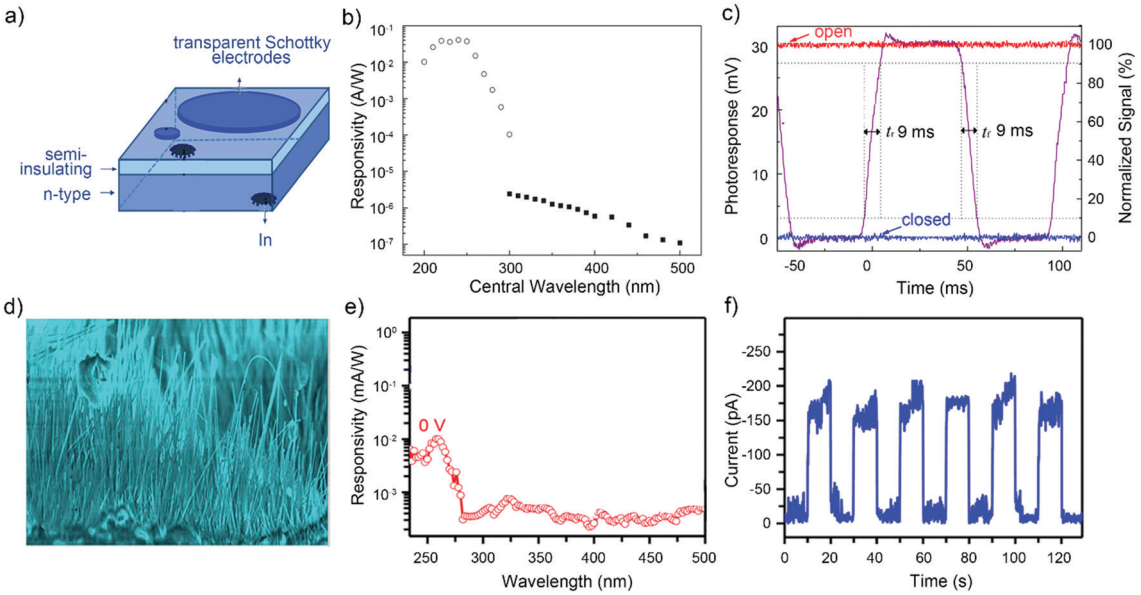

Fig. 8 (a) Schematic, (b) spectral response and (c) transient response of detectors. Reproduced with permission from ref. 110 Copyright 2009 The Japan Society of Applied Physics. (d) An SEM image of Ga_2O_3 nanowire array films, (e) spectral response and (f) time-dependent photocurrent response of devices at zero bias. Reproduced with permission from ref. 111 Copyright 2016 American Chemical Society.

Table 4 Parameter summary list of photovoltaic Ga_2O_3 heterogeneous PN detectors

Type I	Type II	Growth method	Photo-responsivity (A W^{-1})	Quantum efficiency (%)	Rise time (s)	Decay time (s)	Ref.	Time
Photovoltaic heterogeneous PN junctions	GaN/Ga_2O_3	MOCVD	0.0001				96	2011
	4H-SiC/Ga_2O_3	LMBE	0.001		0.65	1.73	98	2016
	p-Si/Ga_2O_3	PLD	0.01				101	2016
	Ga:ZnO/Ga_2O_3	LMBE	0.000763		0.179	0.272	102	2017
	NSTO/Ga_2O_3	RFMS	0.0026	1.3	0.21	0.07	104	2017
	GaN/Ga_2O_3	PLD	0.054		0.1	0.08	93	2017
	ZnO/Ga_2O_3	CVD	0.0097		<0.0001	<0.0009	94	2017
	Diamond/Ga_2O_3	PECVD	0.0002				95	2018
	GaN/Sn:Ga_2O_3	PLD	3.05			0.018	91	2018
	MoS_2/Ga_2O_3		0.00205				107	2018
	HSL/Ga_2O_3	RFMS			0.0322	0.078	112	2018
Photovoltaic Schottky junctions	PEDOT–PSS/Ga_2O_3	Floating zone method	0.037	18	0.009	0.009	110	2009
	Au/Ga_2O_3	Partial thermal oxidation	0.00001		0.000001	0.000064	111	2016
	Graphene/Ga_2O_3/graphene	LMBE	0.7				105	2017
	PEDOT–PSS/Ga_2O_3/Si	MOCVD	0.012	15	0.06	0.088	113	2019

of an appropriate external electric field on the basis of the built-in electric field facilitates the separation of electron–hole pairs, and the response time can be effectively improved by reducing the carrier transit time and diode capacitance. When the applied reverse bias is sufficiently large, electric fields can provide sufficient energy for photo-generated electrons to initiate collision ionization, which can result in avalanche multiplication or breakdown of the photodiode, thus providing sufficient internal current gain.

3.3.1 Heterogeneous PN junctions working under forward or reverse bias. In addition to the abovementioned heterogeneous PN junctions working in the photovoltaic mode, in this section, some of the p-type materials and PN junction photodiodes, which are composed of Ga_2O_3, operating in the non-photovoltaic mode have been discussed.

SiC is characterized by a higher breakdown electric field. It has a smaller drift region (*i.e.*, lower drift region resistance), higher thermal conductivity for better heat dissipation, and wide band gap energy (2.9 eV) to allow operation at higher junction temperatures, which is very suitable for UV applications.[12] In 2016, Qu *et al.*[98] resorted to laser molecular beam epitaxy (L-MBE) technology to epitaxially grow the Ga_2O_3 films on n-type 4H-SiC substrates and thereby fabricated Ga_2O_3/4H-SiC heterojunctions. By replacing the Au/Ti electrodes on the heterojunctions with a single transparent graphene layer, the performance of the device was significantly improved because the transparent graphene layer significantly increased the number of incident photons and provided carrier transmission channel for the separated electrons–holes (Fig. 9).

The graphene film has a unique combination of high electrical conductivity and optical transparency in the UV region.[119]

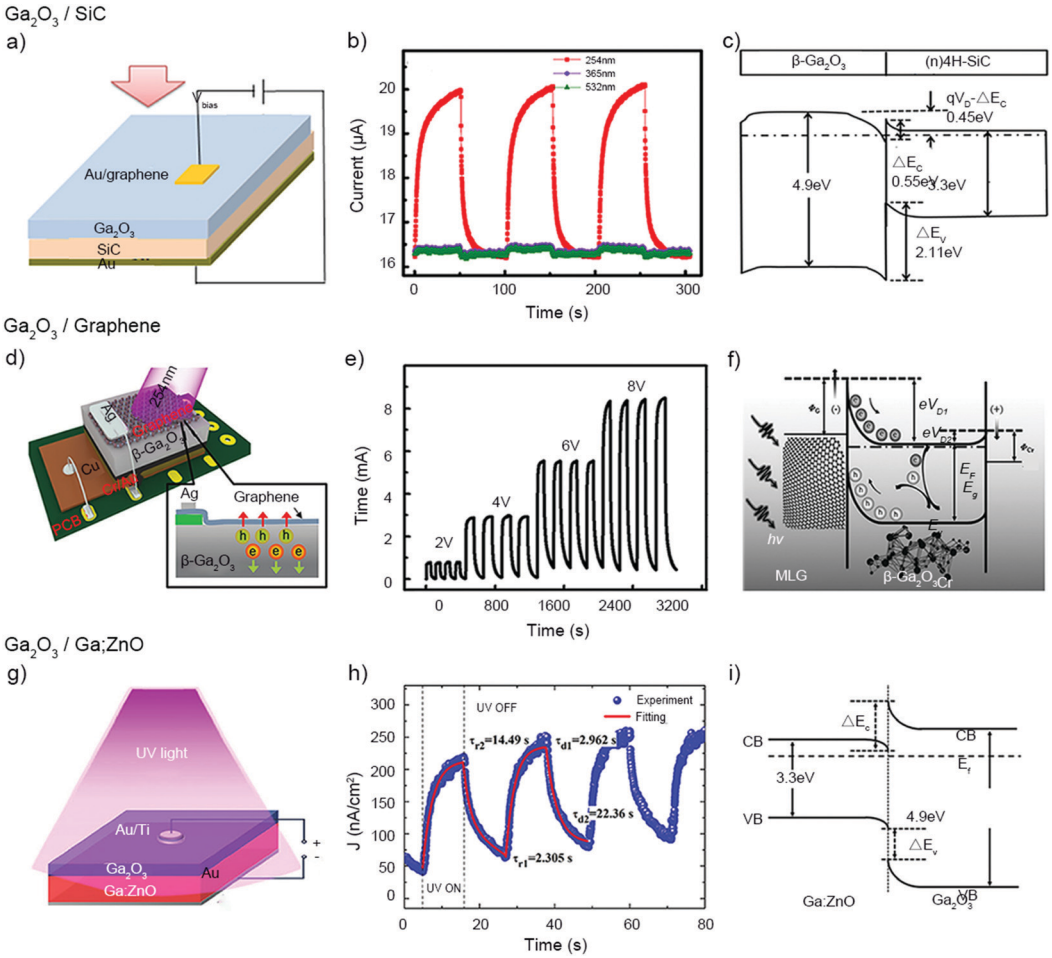

Fig. 9 (a) Schematic, (b) time-dependent photo-response and (c) proposed band structure of Ga_2O_3/4H-SiC UV photodetectors. Reproduced with permission from ref. 98 Copyright 2016 Elsevier B.V. (d) Schematic, (e) time-dependent and bias-dependent photo-response, and (f) energy-band diagram of the MLG/Ga_2O_3 wafer DUVPDs. Reproduced with permission from ref. 106 Copyright 2016 WILEY-VCH Verlag GmbH & Co. KGaA, Weinheim. (g) Schematic, (h) time-dependent photo-response, and i) energy-band diagram of heterojunction-type photodetectors. Reproduced with permission from ref. 102 Copyright 2017 Royal Society of Chemistry.

In 2016, Kong *et al.*[106] combined Sn-atom-doped n-type single-crystal Ga_2O_3 wafers with graphene grown by CVD and then attached an Ag electrode to one end of graphene and a Cr/Au electrode to one end of Ga_2O_3 that were mounted on a printed circuit board to form a photodiode. Under the bias voltage of 20 V, the measured responsivity was 39.3 A W^{-1}, the detectivity was 5.92×10^{13} Jones, and the external quantum efficiency was up to 1.98×10^4%, whereas the response time reached the 10^2 level (Fig. 10).

Generally, due to the large lattice mismatch and the formation of rotation domains, the obtained Ga_2O_3 films have many defects and dislocations; therefore, it is necessary to select suitable substrates for photodiodes. In 2017, Wu *et al.*[102] introduced the lattice-compatible semiconductor Ga:ZnO, used it as a substrate and then fabricated a Ga_2O_3/Ga:ZnO heterojunction detector *via* the L-MBE technology. The photo-responsivity of this diode reached the peak value of 0.76 mA W^{-1} around 260 nm, the light–dark ratio was 2.6×10^2, and the rise/decay response time was 0.179 s/0.272 s.

3.3.2 PIN junctions working under reverse bias. The PIN photodiodes are doped with a layer of n-type semiconductors with low concentration in the PN junctions of photodiodes such that the width of the depletion region can be increased to reduce the influence of diffusion motion and improve the response speed. Since this doped layer is of low doping concentration, which is close to an intrinsic semiconductor, it is called the I layer, and thus, this structure becomes the PIN photodiode. The I layer was thicker, almost occupying the entire depletion region. Most of the incident light was absorbed in the I layer, and a large number of electron–hole pairs were generated. On both sides of the I layer were p-type and n-type semiconductors with high doping concentrations. The p layer and the n layer were very thin, and the proportion of the absorbed incident light was low. Therefore, the drift component of the photoelectric current occupies the dominant position, which greatly improves the response speed.

Researchers have made successful attempts at fabricating solar-blind UV PIN photodiode detectors. In 2016, An *et al.*[120] fabricated p-Si/n-Ga_2O_3 heterojunctions and p-Si/i-SiC/n-Ga_2O_3

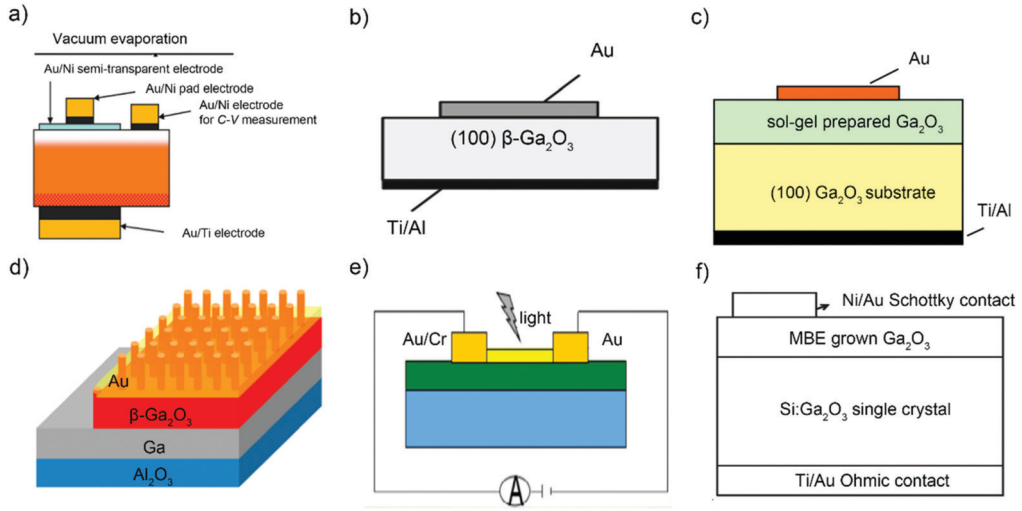

Fig. 10 Schematic of the Au/Ga_2O_3 photodetectors. Reproduced with permission from ref. 111 Copyright 2016 American Chemical Society, ref. 114 Copyright 2008 The Japan Society of Applied Physics, ref. 115 Copyright 2009 American Institute of Physics, ref. 116 Copyright 2011 American Institute of Physics, ref. 117 Copyright 2014 Elsevier B.V. and ref. 118 Copyright 2016 Chinese Physical Society and IOP Publishing Ltd.

heterojunctions by the L-MBE technology and compared the performance of these two heterojunctions. To improve the quality of the p-Si/i-SiC/n-Ga_2O_3 heterojunctions, the research team reduced the oxygen vacancy by changing the oxygen pressure during the retreat. As a result, the rectification ratio of the p-Si/i-SiC/n-Ga_2O_3 heterojunctions was 36 at 4.5 V, the photoelectric responsivity was 5.4×10^5% at −4.5 V, and the wavelength of the irradiated light was 254 nm. Compared to that of the p-Si/n-Ga_2O_3 heterojunctions, the dark current of the p-Si/i-SiC/n-Ga_2O_3 heterojunctions was reduced by three orders of magnitude, and the rectification behaviour was changed from reverse to forward.

3.3.3 Schottky junctions working under bias. Since the energy-band is bent, there are barriers at the interface; the Schottky barrier can operate in the photovoltaic mode. However, to improve responsivity, most Schottky barriers work under bias to achieve higher performance.

It can be seen from the table that the metal of Schottky junctions formed by Ga_2O_3 under bias voltage is mainly Au,[111,114–118] and in a few Schottky junctions, Ni,[121] graphene,[105] and so on are used. In 2008, Oshima *et al.*[114] prepared Schottky-type solar-blind UV detectors based on (100) oriented Ga_2O_3 single crystals. The group first conducted thermal annealing for Ga_2O_3 single crystals to stabilize the oxygen vacancy on the surface and form a high-resistance layer. Then, the Au/Ni and Au/Ti electrodes were used on the surface and back of the substrates to respectively form Schottky and ohmic contact.

The device has the rectification ratio of 10^6 at ±3 V, a deep ultraviolet photoelectric response under negative bias, and the photo-responsivity of 2.6–8.7 A W^{-1} under the illumination of 200–260 nm.

3.3.4 Heterogeneous junctions working in the avalanche mode. Avalanche photodiode (APD) is a pn-junction-type photodiode that utilizes the avalanche multiplication effect of carriers to amplify photoelectric signals and thereby improve the sensitivity of detection. By coupling the pn junction with suitable high reverse bias voltage, the photo-generated carriers in the depletion layer were accelerated by the strong electric field to obtain sufficient kinetic energy, generating new electron–hole pairs with lattice collision ionization. These carriers continuously cause new collision ionization, resulting in the avalanche multiplication of carriers to obtain current gain (Table 5).

The process of avalanche multiplication is shown in the figure. Photons absorbed at point 1 generate electron–hole pairs. Electrons accelerate under the action of a strong electric field. The acceleration process is interrupted by random collisions with electrons, in which the electrons lose some of the obtained energy, and these competitive processes lead to the average saturation speed of electrons. An electron can receive enough kinetic energy such that it can destroy the lattice bond and produce a second electron–hole pair when it collides with atoms. This is called collision ionization (at point 2). The newly generated electrons and holes derive kinetic energy from the field and generate additional electron–hole pairs (*e.g.*, at point 3), which in turn continue the process and create other electron–hole pairs. This process is therefore called avalanche multiplication (Fig. 11).

Due to the weak solar-blind signals, it is necessary to develop solar-blind avalanche photodiodes with high internal avalanche gain. In 2017, Chen *et al.*[122] epitaxially grew single-crystal α-Ga_2O_3 thin films on the non-polar ZnO ($11\bar{2}0$) crystal plane by laser molecular beam epitaxy and prepared a high-performance Schottky-barrier avalanche diode based on the Au/α-Ga_2O_3/ZnO heterojunction structure. The device was self-powered, with the dark current of the pA level at 0 V bias, rejection ratio for UV/visible photo-responsivity of 10^3 and detectivity of 9.66×10^{12} cm $Hz^{1/2}$ W^{-1}. Under the bias voltage of −5 V, the detector was a dual-band response device, the peak wavelength of photo-responsivity was at 255 nm and 365 nm,

Table 5 Parameter summary list of non-photovoltaic Ga_2O_3 heterogeneous PN detectors

Type I	Type II	Growth method	Bias (V)	Photo-responsivity (A W^{-1})	Quantum efficiency (%)	Rise time (s)	Decay time (s)	Ref.	Time
Non-photovoltaic PN junctions	GaN/Ga_2O_3	MOCVD	−10	10				96	2011
	SiC/Ga_2O_3	Oxygen plasma	−2	0.07		0.0012	0.0015	99	2013
	GaN/Ga_2O_3	Oxygen plasma	2	0.1				97	2015
	SiC/Ga_2O_3	LMBE	−5			2.4	1.8	100	2016
	p-Si/Ga_2O_3	PLD	−3	370	180 000	1.79	0.27	101	2016
	4H-SiC/Ga_2O_3	LMBE	−5	0.18		0.65	1.73	98	2016
	Graphene/Ga_2O_3		20	39.3	19 600	95	219	106	2016
	ZnO/Ga_2O_3	RFMS	−5	0.35	170	1.07	0.79	103	2017
	HSL/Ga_2O_3	RFMS	5	96.13	47 600	0.032	0.078	112	2018
	Mg:Ga_2O_3/n-Si	MOCVD	3	0.14		0.02	0.15	123	2019
Non-photovoltaic PIN junctions	p-Si/i-SiC/n-Ga_2O_3	LMBE	−4.5					120	2016
Non-photovoltaic Schottky junctions	Au/Ni/Ga_2O_3	Floating zone method	10	2.6–8.7				114	2008
	Au/Ga_2O_3	Floating zone method	3	1000				115	2009
	Au/Ga_2O_3	Floating zone method	3	4.3	21			116	2011
	Au/Ga_2O_3	Partial thermal oxidation	−10	0.0006		0.000001	0.000064	111	2016
	Au/Ga_2O_3 micro/nano-sheet	CVD	1	19.3	9400	0.02	0.023	117	2015
	Au/Ga_2O_3	MBE	3.8	1.8	870			118	2015
	Ni/Ga_2O_3	EDFG	6	>8				121	2016
	Graphene/Ga_2O_3/graphene	CVD	10	9.66		0.96	0.81	105	2017
Junctions in avalanche mode	SnO_2/Ga_2O_3	RF sputtering	−5.5	2300	4 480 000	0.000025	0.000048	124	2016
	ZnO/α-Ga_2O_3	LMBE	−40	11 000		< 0.00005	0.000238	122	2017

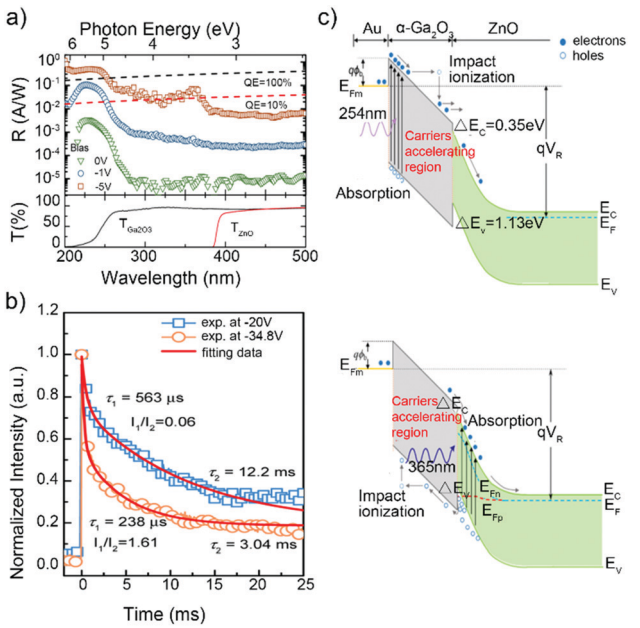

Fig. 11 (a) Spectral photoresponse of a 400 μm diameter Schottky diode under different biases, and the transmittance spectra of the Ga_2O_3 epilayer and ZnO substrate. (b) Normalized transient photoresponse characteristics of the detector. (c) Schematic energy diagrams at high reverse bias under 254 and 365 nm illumination. Reproduced with permission from ref. 122 Copyright 2017 American Chemical Society.

and the corresponding photo-responsivity was 0.50 A W^{-1} and 0.071 A W^{-1}. At a bias of −40 V, the device exhibited high avalanche gain, and the photo-responsivity to 254 nm deep ultraviolet light was as high as 1×10^4 A W^{-1}, with total gain exceeding 10^5.

4 Discussion and expectation

Via the abovementioned discussion, we learned about the development of solar-blind UV photodetectors as well as heterogeneous PN junction and Schottky junction detectors working in the photovoltaic mode and non-photovoltaic modes. Each of them has its own pros and cons and complements each other.

To date, although the performances of Ga_2O_3-based solar-blind UV detectors have been gradually improved, they are not satisfactory from a practical point of view. In general, the detectors made of wide band gap semiconductors have several problems: low conductivity, large dislocation densities and cracking of the deposited film due to the thermal/lattice expansion mismatches.[125] On this basis, researchers have come up with several ways to solve the abovementioned problems: avalanche gain (as abovementioned), energy-band regulation, homogenous PN junctions and so on. In addition, the author believes that the further development of Ga_2O_3 detection needs to focus on the breakthroughs of energy-band engineering and Ga_2O_3 homogenous PN junctions.

4.1 Energy band engineering

We know that Ga_2O_3 has the bandgap of 4.9 eV (corresponding to the absorption cut-off wavelength of 250 nm). In fact, when put into practical use, an ideal solar-blind UV detector should have the optimal photo-response cut-off wavelength of 280 nm, which can ensure the farthest information transmission without background interference. To obtain the ideal absorption cut-off edge of 280 nm, energy band engineering has been widely used in GaN and ZnO materials. The most mainstream representatives are $Al_{0.38}Ga_{0.62}N$[11] and $Mg_{0.52}Zn_{0.48}O$.[13] However, there are few studies on Ga_2O_3 energy-band engineering,

especially on the potential InGaO materials. Therefore, research on the InGaO materials will become a potentially hot topic in the field of solar-blind UV detection in the future.

Material energy-band regulation refers to combining two materials of different band gaps by some method and adjusting the composition of these two materials to achieve the expected value between two band gap values. In the energy-band engineering of solar-blind UV detectors, researchers have widely used $Al_xGa_{1-x}N$[29,30] and $Mg_xZn_{1-x}O$.[31,32] However, when the components of Al and Mg are respectively added to achieve the conditions of solar-blind ultraviolet detection, deterioration of the film quality of AlGaN and phase segregation of MgZnO occur, which make them challenging to be put into practical use currently.[126] Therefore, researchers have focused their attention on Ga_2O_3.

Due to the wide band gap of the Ga_2O_3 materials, the detectors made with these materials cover most of the areas of solar-blind UV bands. By incorporating other elements, such as Er,[127] Al,[128] Zn,[126] Mg[129] and In,[130] into Ga_2O_3 and adjusting the ratio, it is possible to adjust the cut-off wavelength of the detector. In addition, a wider band gap engineering is the key to achieve higher breakdown voltage, thereby facilitating the large-scale production of photodetectors and improving the frequency response characteristics of the devices.[128]

4.2 Ga_2O_3 homogeneous PN junction

At present, as a stable doping technology of Ga_2O_3 has not been developed, the current mainstream solution we summarized above is to avoid homogenous pn technology and instead use heterojunctions. As is well-known, semiconductor heterojunctions are not the most ideal device structure because of the important constraints that affect the device: for example, lattice mismatch, effective mismatch or energy band bending. Therefore, the p-type doping technology of Ga_2O_3 and the homogeneous pn junction device will be the focus of future development and the bottleneck worth breaking through.

Homogeneous junctions are classified into metal/metal and semiconductor/semiconductor homojunctions. It is important to emphasize that metal/metal and semiconductor/semiconductor homojunctions are formed by covalent coupling of the same metal or semiconductor components (rather than intermolecular or hydrogen bonding), and these homojunctions have good stability.[131]

Ga_2O_3, a promising candidate in next-generation electronics, belongs to the semiconductor category. However, due to the existence of the self-compensation process, the realization of p-type conductive Ga_2O_3 faces enormous challenges, which is crucial for the further expansion of its application and promotion. At present, to the best of our knowledge, in addition to homogenous junctions made of different nano-morphologies of Ga_2O_3,[132] it is theoretically possible to reduce the oxygen vacancy using divalent ions (Zn[133,134] and Mg[129]) and thereby form p-type Ga_2O_3. In 2019, Su *et al.*[135] fabricated Zn-doped and Zn–Mg co-doped Ga_2O_3 thin films by radiation frequency magnetron, thereby investigating the acceptor levels of ZnGa and MgGa. The experimental results show that the acceptor levels of ZnGa and MgGa are 0.79 eV and 1.00 eV, respectively. These high values indicate why it is difficult to obtain highly conductive p-type Ga_2O_3 by doping Zn and Mg impurities.

Conflicts of interest

The authors declare no competing financial interest.

Acknowledgements

This work was financially supported by the National Natural Science Foundation of China (Grant No. 61604178, 61427901, U1505252, and 91833301).

Notes and references

1 W. Zheng, F. Huang, R. Zheng and H. Wu, *Adv. Mater.*, 2015, **27**, 3921–3927.
2 W. Zheng, R. Lin, L. Jia and F. Huang, *Photonics Res.*, 2019, **7**, 98–102.
3 W. Zheng, R. Lin, J. Ran, Z. Zhang, X. Ji and F. Huang, *ACS Nano*, 2018, **12**, 425–431.
4 W. Zheng, R. Lin, Y. Zhu, Z. Zhang, X. Ji and F. Huang, *ACS Appl. Mater. Interfaces*, 2018, **10**, 20696–20702.
5 R. Lin, W. Zheng, D. Zhang, Z. Zhang, Q. Liao, L. Yang and F. Huang, *ACS Appl. Mater. Interfaces*, 2018, **10**, 22419–22426.
6 W. Zheng, R. Lin, D. Zhang, L. Jia, X. Ji and F. Huang, *Adv. Opt. Mater.*, 2018, **6**, 1800697.
7 P. Schreiber, T. Dang, T. Pickenpaugh, G. A. Smith, P. Gehred and C. W. Litton, *Proc. SPIE*, 1999, **3629**, 230.
8 D. Zhang, W. Zheng, Q. Zheng, A. Chen, X. Ji and F. Huang, *Adv. Electron. Mater.*, 2016, **2**, 1600320.
9 W. Zheng, Z. Zhang, R. Lin, K. Xu, J. He and F. Huang, *Adv. Electron. Mater.*, 2016, **2**, 1600291.
10 Q. Hu, W. Zheng, R. Lin, Y. Xu and F. Huang, *Carbon*, 2019, **147**, 427–433.
11 H. Kan, W. Zheng, R. Lin, M. Li, C. Fu, H. Sun, M. Dong, C. Xu, J. Luo, Y. Fu and F. Huang, *ACS Appl. Mater. Interfaces*, 2019, **11**, 8412–8418.
12 M. Razeghi and A. Rogalski, *J. Appl. Phys.*, 1996, **79**, 7433–7473.
13 W. Zheng, X. Xiong, R. Lin, Z. Zhang, C. Xu and F. Huang, *ACS Appl. Mater. Interfaces*, 2018, **10**, 1865–1870.
14 Z. Zhang, W. Zheng, R. Lin and F. Huang, *R. Soc. Open Sci.*, 2018, **5**, 180905.
15 C. Xu, Z. Du, Y. Huang, M. Dong, R. Lin, Y. Li, B. Wang, W. Zheng and F. Huang, *ACS Appl. Mater. Interfaces*, 2018, **10**, 42681–42687.
16 Y.-J. Lu, C.-N. Lin and C.-X. Shan, *Adv. Opt. Mater.*, 2018, **6**, 1800359.
17 W. Zheng, R. Lin, Z. Zhang and F. Huang, *ACS Appl. Mater. Interfaces*, 2018, **10**, 27116–27123.
18 Z. Alaie, S. Mohammad Nejad and M. H. Yousefi, *Mater. Sci. Semicond. Process.*, 2015, **29**, 16–55.

19 M. Dong, W. Zheng, C. Xu, R. Lin, D. Zhang, Z. Zhang and F. Huang, *Adv. Opt. Mater.*, 2019, **7**, 1801272.
20 W. Zheng, R. Lin, Z. Zhang, Q. Liao, J. Liu and F. Huang, *Nanoscale*, 2017, **9**, 12718–12726.
21 P. Glasow, G. Ziegler, W. Suttrop, G. Pensl and R. Helbig, *Proc. SPIE*, 1988, **0868**, 40.
22 M. Liao, Y. Koide and J. Alvarez, *Appl. Phys. Lett.*, 2005, **87**, 022105.
23 Y. Koide, M. Liao and J. Alvarez, *Diamond Relat. Mater.*, 2006, **15**, 1962–1966.
24 R. Dahal, J. Li, Z. Y. Fan, M. L. Nakarmi, T. M. A. Tahtamouni, J. Y. Lin and H. X. Jiang, *Phys. Status Solidi C*, 2008, **5**, 2148–2151.
25 W. Zheng, R. Zheng, F. Huang, H. Wu and F. Li, *Photonics Res.*, 2015, **3**, 38–43.
26 W. Zheng, R. S. Zheng, H. L. Wu and F. Di Li, *J. Alloys Compd.*, 2014, **584**, 374–376.
27 A. Soltani, H. A. Barkad, M. Mattalah, B. Benbakhti, J. C. De Jaeger, Y. M. Chong, Y. S. Zou, W. J. Zhang, S. T. Lee, A. BenMoussa, B. Giordanengo and J. F. Hochedez, *Appl. Phys. Lett.*, 2008, **92**, 053501.
28 L. Bugallo Ade, M. Tchernycheva, G. Jacopin, L. Rigutti, F. H. Julien, S. T. Chou, Y. T. Lin, P. H. Tseng and L. W. Tu, *Nanotechnology*, 2010, **21**, 315201.
29 N. Biyikli, O. Aytur, I. Kimukin, T. Tut and E. Ozbay, *Appl. Phys. Lett.*, 2002, **81**, 3272–3274.
30 M. Razeghi, *Proc. IEEE*, 2002, **90**, 1006–1014.
31 I. Takeuchi, W. Yang, K. S. Chang, M. A. Aronova, T. Venkatesan, R. D. Vispute and L. A. Bendersky, *J. Appl. Phys.*, 2003, **94**, 7336–7340.
32 S. Han, Z. Zhang, J. Zhang, L. Wang, J. Zheng, H. Zhao, Y. Zhang, M. Jiang, S. Wang, D. Zhao, C. Shan, B. Li and D. Shen, *Appl. Phys. Lett.*, 2011, **99**, 242105.
33 W. Zheng, Z. C. Feng, J.-F. Lee, D.-S. Wuu and R. S. Zheng, *J. Alloys Compd.*, 2014, **582**, 157–160.
34 C. Xie and F. Yan, *Small*, 2017, **13**, 1701822.
35 Z. Ji, J. Du, J. Fan and W. Wang, *Opt. Mater.*, 2006, **28**, 415–417.
36 P. Feng, J. Y. Zhang, Q. H. Li and T. H. Wang, *Appl. Phys. Lett.*, 2006, **88**, 153107.
37 T. Oshima, T. Okuno and S. Fujita, *Jpn. J. Appl. Phys.*, 2007, **46**, 7217–7220.
38 D. Guo, Z. Wu, P. Li, Y. An, H. Liu, X. Guo, H. Yan, G. Wang, C. Sun, L. Li and W. Tang, *Opt. Mater. Express*, 2014, **4**, 1067.
39 D. Y. Guo, Z. P. Wu, Y. H. An, X. C. Guo, X. L. Chu, C. L. Sun, L. H. Li, P. G. Li and W. H. Tang, *Appl. Phys. Lett.*, 2014, **105**, 023507.
40 X. Z. Liu, P. Guo, T. Sheng, L. X. Qian, W. L. Zhang and Y. R. Li, *Opt. Mater.*, 2016, **51**, 203–207.
41 L. X. Qian, X. Z. Liu, T. Sheng, W. L. Zhang, Y. R. Li and P. T. Lai, *AIP Adv.*, 2016, **6**, 045009.
42 D. Guo, P. Li, Z. Wu, W. Cui, X. Zhao, M. Lei, L. Li and W. Tang, *Sci. Rep.*, 2016, **6**, 24190.
43 D. Y. Guo, X. L. Zhao, Y. S. Zhi, W. Cui, Y. Q. Huang, Y. H. An, P. G. Li, Z. P. Wu and W. H. Tang, *Mater. Lett.*, 2016, **164**, 364–367.
44 X. Zhao, Y. Zhi, W. Cui, D. Guo, Z. Wu, P. Li, L. Li and W. Tang, *Opt. Mater.*, 2016, **62**, 651–654.
45 A. Singh Pratiyush, S. Krishnamoorthy, S. Vishnu Solanke, Z. Xia, R. Muralidharan, S. Rajan and D. N. Nath, *Appl. Phys. Lett.*, 2017, **110**, 221107.
46 L. X. Qian, Y. Wang, Z. H. Wu, T. Sheng and X. Z. Liu, *Vacuum*, 2017, **140**, 106–110.
47 P. Ravadgar, R. H. Horng, S. D. Yao, H. Y. Lee, B. R. Wu, S. L. Ou and L. W. Tu, *Opt. Express*, 2013, **21**, 24599–24610.
48 G. C. Hu, C. X. Shan, N. Zhang, M. M. Jiang, S. P. Wang and D. Z. Shen, *Opt. Express*, 2015, **23**, 13554–13561.
49 S. Oh, Y. Jung, M. A. Mastro, J. K. Hite, C. R. Eddy Jr. and J. Kim, *Opt. Express*, 2015, **23**, 28300–28305.
50 S. Rafique, L. Han and H. Zhao, *Phys. Status Solidi A*, 2017, **214**, 1700063.
51 D. Zhang, W. Zheng, R. C. Lin, T. T. Li, Z. J. Zhang and F. Huang, *J. Alloys Compd.*, 2018, **735**, 150–154.
52 R. Lin, W. Zheng, D. Zhang, Z. Zhang, Q. Liao, L. Yang and F. Huang, *ACS Appl. Mater. Interfaces*, 2018, **10**, 22419–22426.
53 Y. Xu, Z. An, L. Zhang, Q. Feng, J. Zhang, C. Zhang and Y. Hao, *Opt. Mater. Express*, 2018, **8**, 2941.
54 Y. Li, D. Zhang, R. Lin, Z. Zhang, W. Zheng and F. Huang, *ACS Appl. Mater. Interfaces*, 2019, **11**, 1013–1020.
55 M. Pavesi, F. Fabbri, F. Boschi, G. Piacentini, A. Baraldi, M. Bosi, E. Gombia, A. Parisini and R. Fornari, *Mater. Chem. Phys.*, 2018, **205**, 502–507.
56 Y.-C. Chen, Y.-J. Lu, Q. Liu, C.-N. Lin, J. Guo, J.-H. Zang, Y.-Z. Tian and C.-X. Shan, *J. Mater. Chem. C*, 2019, **7**, 2557–2562.
57 Y. An, X. Chu, Y. Huang, Y. Zhi, D. Guo, P. Li, Z. Wu and W. Tang, *Prog. Nat. Sci.: Mater. Int.*, 2016, **26**, 65–68.
58 L.-X. Qian, Z.-H. Wu, Y.-Y. Zhang, P. T. Lai, X.-Z. Liu and Y.-R. Li, *ACS Photonics*, 2017, **4**, 2203–2211.
59 S. Cui, Z. Mei, Y. Zhang, H. Liang and X. Du, *Adv. Opt. Mater.*, 2017, **5**, 1700454.
60 Y. Peng, Y. Zhang, Z. Chen, D. Guo, X. Zhang, P. Li, Z. Wu and W. Tang, *IEEE Photonics Technol. Lett.*, 2018, **30**, 993–996.
61 Y. Kokubun, K. Miura, F. Endo and S. Nakagomi, *Appl. Phys. Lett.*, 2007, **90**, 031912.
62 H. Shen, Y. Yin, K. Tian, K. Baskaran, L. Duan, X. Zhao and A. Tiwari, *J. Alloys Compd.*, 2018, **766**, 601–608.
63 W. Y. Weng, T. J. Hsueh, S. J. Chang, G. J. Huang and H. T. Hsueh, *IEEE Sens. J.*, 2011, **11**, 999–1003.
64 Z.-D. Huang, W. Y. Weng, S. J. Chang, C.-J. Chiu, T.-J. Hsueh and S.-L. Wu, *IEEE Sens. J.*, 2013, **13**, 3462–3467.
65 Z.-D. Huang, W.-Y. Weng, S.-J. Chang, Y.-F. Hua, C.-J. Chiu, T.-J. Hsueh and S.-L. Wu, *IEEE Sens. J.*, 2013, **13**, 1187–1191.
66 D. Patil-Chaudhari, M. Ombaba, J. Y. Oh, H. Mao, K. H. Montgomery, A. Lange, S. Mahajan, J. M. Woodall and M. S. Islam, *IEEE Photonics J.*, 2017, **9**, 1–7.
67 F.-P. Yu, S.-L. Ou and D.-S. Wuu, *Opt. Mater. Express*, 2015, **5**, 1240.
68 P. Jaiswal, U. Ul Muazzam, A. S. Pratiyush, N. Mohan, S. Raghavan, R. Muralidharan, S. A. Shivashankar and D. N. Nath, *Appl. Phys. Lett.*, 2018, **112**, 021105.

69 S. H. Lee, K. M. Lee, Y.-B. Kim, Y.-J. Moon, S. B. Kim, D. Bae, T. J. Kim, Y. D. Kim, S.-K. Kim and S. W. Lee, *J. Alloys Compd.*, 2019, **780**, 400–407.
70 L. X. Qian, H. Y. Liu, H. F. Zhang, Z. H. Wu and W. L. Zhang, *Appl. Phys. Lett.*, 2019, **114**, 113506.
71 B. R. Tak, M. Garg, S. Dewan, C. G. Torres-Castanedo, K.-H. Li, V. Gupta, X. Li and R. Singh, *J. Appl. Phys.*, 2019, **125**, 144501.
72 H. Aida, K. Nishiguchi, H. Takeda, N. Aota, K. Sunakawa and Y. Yaguchi, *Jpn. J. Appl. Phys.*, 2008, **47**, 8506–8509.
73 W. Mu, Z. Jia, Y. Yin, Q. Hu, J. Zhang, Q. Feng, Y. Hao and X. Tao, *CrystEngComm*, 2017, **19**, 5122–5127.
74 Q. Feng, L. Huang, G. Han, F. Li, X. Li, L. Fang, X. Xing, J. Zhang, W. Mu, Z. Jia, D. Guo, W. Tang, X. Tao and Y. Hao, *IEEE Trans. Electron Devices*, 2016, **63**, 3578–3583.
75 X. Chen, W. Mu, Y. Xu, B. Fu, Z. Jia, F.-F. Ren, S. Gu, R. Zhang, Y. Zheng, X. Tao and J. Ye, *ACS Appl. Mater. Interfaces*, 2019, **11**, 7131–7137.
76 Y. Li, T. Tokizono, M. Liao, M. Zhong, Y. Koide, I. Yamada and J.-J. Delaunay, *Adv. Funct. Mater.*, 2010, **20**, 3972–3978.
77 L. Li, E. Auer, M. Liao, X. Fang, T. Zhai, U. K. Gautam, A. Lugstein, Y. Koide, Y. Bando and D. Golberg, *Nanoscale*, 2011, **3**, 1120–1126.
78 T. He, Y. Zhao, X. Zhang, W. Lin, K. Fu, C. Sun, F. Shi, X. Ding, G. Yu, K. Zhang, S. Lu, X. Zhang and B. Zhang, *Nanophotonics*, 2018, **7**, 1557–1562.
79 W. Feng, X. Wang, J. Zhang, L. Wang, W. Zheng, P. Hu, W. Cao and B. Yang, *J. Mater. Chem. C*, 2014, **2**, 3254–3259.
80 W. Y. Weng, T. J. Hsueh, S. J. Chang, G. J. Huang and S. P. Chang, *IEEE Photonics Technol. Lett.*, 2010, **22**, 709–711.
81 Y. L. Wu, S.-J. Chang, W. Y. Weng, C. H. Liu, T. Y. Tsai, C. L. Hsu and K. C. Chen, *IEEE Sens. J.*, 2013, **13**, 2368–2373.
82 W. Cui, D. Guo, X. Zhao, Z. Wu, P. Li, L. Li, C. Cui and W. Tang, *RSC Adv.*, 2016, **6**, 100683.
83 S. Oh, C.-K. Kim and J. Kim, *ACS Photonics*, 2017, **5**, 1123–1128.
84 Y. Teng, X. Song-le, A. Ponchel, Z. K. Yang and J. Xia, *Adv. Mater.*, 2014, **26**, 6238–6243.
85 R. Zou, Z. Zhang, Q. Liu, J. Hu, L. Sang, M. Liao and W. Zhang, *Small*, 2014, **10**, 1848–1856.
86 J. Zhang, S. Jiao, D. Wang, S. Ni, S. Gao and J. Wang, *J. Mater. Chem. C*, 2019, **7**, 6867–6871.
87 T. Wang, S. S. Farvid, M. Abulikemu and P. V. Radovanovic, *J. Am. Chem. Soc.*, 2010, **132**, 9250–9252.
88 W. Y. Weng, T. J. Hsueh, S.-J. Chang, G. J. Huang and S. C. Hung, *IEEE Trans. Nanotechnol.*, 2011, **10**, 1047–1052.
89 S. Wang, H. Sun, Z. Wang, X. Zeng, G. Ungar, D. Guo, J. Shen, P. Li, A. Liu, C. Li and W. Tang, *J. Alloys Compd.*, 2019, **787**, 133–139.
90 E. G. Víllora, K. Shimamura, Y. Yoshikawa, T. Ujiie and K. Aoki, *Appl. Phys. Lett.*, 2008, **92**, 202120.
91 D. Guo, Y. Su, H. Shi, P. Li, N. Zhao, J. Ye, S. Wang, A. Liu, Z. Chen, C. Li and W. Tang, *ACS Nano*, 2018, **12**, 12827–12835.
92 S. I. Maximenko, L. Mazeina, Y. N. Picard, J. A. Freitas, V. M. Bermudez and S. M. Prokes, *Nano Lett.*, 2009, **9**, 3245–3251.
93 P. Li, H. Shi, K. Chen, D. Guo, W. Cui, Y. Zhi, S. Wang, Z. Wu, Z. Chen and W. Tang, *J. Mater. Chem. C*, 2017, **5**, 10562–10570.
94 B. Zhao, F. Wang, H. Chen, L. Zheng, L. Su, D. Zhao and X. Fang, *Adv. Funct. Mater.*, 2017, **27**, 1700264.
95 Y.-C. Chen, Y.-J. Lu, C.-N. Lin, Y.-Z. Tian, C.-J. Gao, L. Dong and C.-X. Shan, *J. Mater. Chem. C*, 2018, **6**, 5727–5732.
96 W. Y. Weng, T. J. Hsueh, S. J. Chang, G. J. Huang and H. T. Hsueh, *IEEE Photonics Technol. Lett.*, 2011, **23**, 444–446.
97 S. Nakagomi, T.-a. Sato, Y. Takahashi and Y. Kokubun, *Sens. Actuators, A*, 2015, **232**, 208–213.
98 Y. Qu, Z. Wu, M. Ai, D. Guo, Y. An, H. Yang, L. Li and W. Tang, *J. Alloys Compd.*, 2016, **680**, 247–251.
99 S. Nakagomi, T. Momo, S. Takahashi and Y. Kokubun, *Appl. Phys. Lett.*, 2013, **103**, 072105.
100 Y. H. An, D. Y. Guo, S. Y. Li, Z. P. Wu, Y. Q. Huang, P. G. Li, L. H. Li and W. H. Tang, *J. Phys. D: Appl. Phys.*, 2016, **49**, 285111.
101 X. C. Guo, N. H. Hao, D. Y. Guo, Z. P. Wu, Y. H. An, X. L. Chu, L. H. Li, P. G. Li, M. Lei and W. H. Tang, *J. Alloys Compd.*, 2016, **660**, 136–140.
102 Z. Wu, L. Jiao, X. Wang, D. Guo, W. Li, L. Li, F. Huang and W. Tang, *J. Mater. Chem. C*, 2017, **5**, 8688–8693.
103 D. Y. Guo, H. Z. Shi, Y. P. Qian, M. Lv, P. G. Li, Y. L. Su, Q. Liu, K. Chen, S. L. Wang, C. Cui, C. R. Li and W. H. Tang, *Semicond. Sci. Technol.*, 2017, **32**, 03LT01.
104 D. Guo, H. Liu, P. Li, Z. Wu, S. Wang, C. Cui, C. Li and W. Tang, *ACS Appl. Mater. Interfaces*, 2017, **9**, 1619–1628.
105 M. Ai, D. Guo, Y. Qu, W. Cui, Z. Wu, P. Li, L. Li and W. Tang, *J. Alloys Compd.*, 2017, **692**, 634–638.
106 W. Y. Kong, G. A. Wu, K. Y. Wang, T. F. Zhang, Y. F. Zou, D. D. Wang and L. B. Luo, *Adv. Mater.*, 2016, **28**, 10725–10731.
107 R. Zhuo, D. Wu, Y. Wang, E. Wu, C. Jia, Z. Shi, T. Xu, Y. Tian and X. Li, *J. Mater. Chem. C*, 2018, **6**, 10982–10986.
108 J. M. Van Hove, R. Hickman, J. J. Klaassen, P. P. Chow and P. P. Ruden, *Appl. Phys. Lett.*, 1997, **70**, 2282–2284.
109 K.-W. Chang and J.-J. Wu, *J. Phys. Chem. B*, 2005, **109**, 13572–13577.
110 T. Oshima, T. Okuno, N. Arai, N. Suzuki, H. Hino and S. Fujita, *Jpn. J. Appl. Phys.*, 2009, **48**, 011605.
111 X. Chen, K. Liu, Z. Zhang, C. Wang, B. Li, H. Zhao, D. Zhao and D. Shen, *ACS Appl. Mater. Interfaces*, 2016, **8**, 4185–4191.
112 K. Arora, N. Goel, M. Kumar and M. Kumar, *ACS Photonics*, 2018, **5**, 2391–2401.
113 D. Zhang, W. Zheng, R. Lin, Y. Li and F. Huang, *Adv. Funct. Mater.*, 2019, **29**, 1900935.
114 T. Oshima, T. Okuno, N. Arai, N. Suzuki, S. Ohira and S. Fujita, *Appl. Phys. Express*, 2008, **1**, 011202.
115 R. Suzuki, S. Nakagomi, Y. Kokubun, N. Arai and S. Ohira, *Appl. Phys. Lett.*, 2009, **94**, 222102.
116 R. Suzuki, S. Nakagomi and Y. Kokubun, *Appl. Phys. Lett.*, 2011, **98**, 131114.

117 M. Zhong, Z. Wei, X. Meng, F. Wu and J. Li, *J. Alloys Compd.*, 2015, **619**, 572–575.
118 X. Z. Liu, C. Yue, C. T. Xia and W. L. Zhang, *Chin. Phys. B*, 2016, **25**, 017201.
119 P. Gao, K. Ding, Y. Wang, K. Ruan, S. Diao, Q. Zhang, B. Sun and J. Jie, *J. Phys. Chem. C*, 2014, **118**, 5164–5171.
120 Y. An, Y. Zhi, Z. Wu, W. Cui, X. Zhao, D. Guo, P. Li and W. Tang, *Appl. Phys. A: Mater. Sci. Process.*, 2018, **30**, 993–996.
121 A. M. Armstrong, M. H. Crawford, A. Jayawardena, A. Ahyi and S. Dhar, *J. Appl. Phys.*, 2016, **119**, 103102.
122 X. Chen, Y. Xu, D. Zhou, S. Yang, F. F. Ren, H. Lu, K. Tang, S. Gu, R. Zhang, Y. Zheng and J. Ye, *ACS Appl. Mater. Interfaces*, 2017, **9**, 36997–37005.
123 D. Zhang, Z. Du, M. Ma, W. Zheng, S. Liu and F. Huang, *Vacuum*, 2019, **159**, 204–208.
124 W. E. Mahmoud, *Sol. Energy Mater. Sol. Cells*, 2016, **152**, 65–72.
125 R. G. Banal, M. Funato and Y. Kawakami, *Appl. Phys. Lett.*, 2011, **99**, 011902.
126 F. Alema, B. Hertog, O. Ledyaev, D. Volovik, G. Thoma, R. Miller, A. Osinsky, P. Mukhopadhyay, S. Bakhshi, H. Ali and W. V. Schoenfeld, *Phys. Status Solidi A*, 2017, **214**, 1600688.
127 Z. Wu, G. Bai, Y. Qu, D. Guo, L. Li, P. Li, J. Hao and W. Tang, *Appl. Phys. Lett.*, 2016, **108**, 211903.
128 Q. Feng, X. Li, G. Han, L. Huang, F. Li, W. Tang, J. Zhang and Y. Hao, *Opt. Mater. Express*, 2017, **7**, 1240.
129 Y. P. Qian, D. Y. Guo, X. L. Chu, H. Z. Shi, W. K. Zhu, K. Wang, X. K. Huang, H. Wang, S. L. Wang, P. G. Li, X. H. Zhang and W. H. Tang, *Mater. Lett.*, 2017, **209**, 558–561.
130 K.-Y. Chen, C.-C. Hsu, H.-C. Yu, Y.-M. Peng, C.-C. Yang and Y.-K. Su, *IEEE Trans. Electron Devices*, 2018, **65**, 1817–1822.
131 X. Feng, G. Hu and J. Hu, *Nanoscale*, 2011, **3**, 2099–2117.
132 T. I. Shin, H. J. Lee, W. Y. Song, S.-W. Kim, M. H. Park, C. W. Yang and D. H. Yoon, *Nanotechnology*, 2007, **18**, 345305.
133 Q. Feng, J. Liu, Y. Yang, D. Pan, Y. Xing, X. Shi, X. Xia and H. Liang, *J. Alloys Compd.*, 2016, **687**, 964–968.
134 D. Guo, X. Qin, M. Lv, H. Shi, Y. Su, G. Yao, S. Wang, C. Li, P. Li and W. Tang, *Electron. Mater. Lett.*, 2017, **13**, 483–488.
135 Y. Su, D. Guo, J. Ye, H. Zhao, Z. Wang, S. Wang, P. Li and W. Tang, *J. Alloys Compd.*, 2019, **782**, 299–303.